Determination of the strain distribution in the adhesive joints using Fiber Bragg Grating (FBG)

Ana Luísa Correia Dias Loureiro

Dissertação do MIEM

Orientadores: Prof. Lucas Filipe Martins da Silva

Prof. Pedro Miguel Guimarães Pires Moreira

Faculdade de Engenharia da Universidade do Porto

Mestrado Integrado em Engenharia Mecânica

Julho 2011

Resumo

O trabalho apresentado nesta tese consiste no desenvolvimento e teste de uma técnica capaz de medir valores de deformação em pontos no interior de uma junta adesiva. À medida que cada vez mais indústrias adoptam as juntas adesivas como técnica de construção, cresce também a necessidade de implementar métodos capazes de monitorizar e controlar juntas adesivas durante o período de serviço. O método apresentado neste trabalho, baseado em fibras ópticas, pretende proporcionar visualização em tempo-real do estado de deformação de uma junta adesiva.

No início deste trabalho encontra-se a descrição de um procedimento de manufactura de juntas equipadas com sensores de Bragg no seu interior. Juntas de sobreposição simples são então produzidas segundo este método e testadas à tracção. Os resultados destes testes laboratoriais são então comparados com resultados de modelos de elementos finitos de modo a verificar a precisão do processo de medição e ajudar à compreensão do processo de medição. Como passo final, possíveis melhorias ao processo foram sugeridas.

Determination of the strain distribution in adhesive joints using Fiber Bragg Grating (FBG)

Abstract

This work focuses on the development and testing of a technique used to measure strain levels inside an adhesive joint. As more industries adopt high performance structural adhesives, the need for structural monitoring and quality control of adhesive joints rises. The method presented in this work, based on optic fibers, is proposed as a possible mean for real-time health monitoring of adhesive connections. In the first part of this work a procedure for embedding optical fibers etched with Bragg sensors is explained. Instrumented, single lap joints were manufactured and subjected to tensile test. The results were compared with finite element models to ensure the accuracy and provide a better understanding of the measurement process. Lastly, improvements to the procedure were suggested.

Acknowledgments

The author would like to thank the support of all people who accompanied her during this work, specially:

Dr Lucas da Silva

Dr Pedro Moreira

Dr Jaime Monteiro

Dr António de Magalhães

Sika® Portugal

FiberSensing®

Mr Miguel Figueiredo

Mr Raul Campilho

Mr José Alexandre Neto

Mr Filipe Chaves

Mr Eduardo Marques

Ms Mariana Banea

Mr Ricardo Carbas

Mr Rui Silva

Ms Diana Viegas

Ms Emília Soares

Index

Figure index

Table index

1. Introduction

Adhesive bonding is a material joining technique widely used in various industries that require strong, light and durable connections. The aerospace and automotive industries are the most important industries using this technology, employing it to build lightweight structures and vehicles that enable simultaneously reduced energy consumption and high safety standards. One of the main advantages of adhesive joints is the existence of a uniform stress distribution along the bonded region, especially when compared with other traditional joining methods such as rivets or fasteners. However, even in the most favorable joint geometries, this stress distribution is not perfectly uniform, with peaks near the ends of the bonded section. It is very important to understand how the stress/strain is distributed to optimize the joint geometry. Having an accurate idea of the stress/strain distribution is not only useful during the design phase but also during the service phase. Adhesive bonding is in various aspects very different from the conventional joining techniques and the manufacturing parameters have large influence on the joint strength. This creates difficulties in producing a consistently strong joint. Having access to a method able to continuously monitor the performance of an adhesive joint can be a powerful and helpful tool that allows the design of stronger and trustworthy joints.

1.1 Definition of the problem

Conventional methods for stress/strain measurement work very poorly for measuring strain in adhesive layers. The thin bondlines used in this type of connection (0.05 to 0.5 mm) make the use of strain gauge based methods impossible, as there is simply not sufficient area to mount the gauge. Optical methods that rely in analyzing images of the surface also have extremely small areas to work with as well due to the typically rough surface found in the fillets of the adhesive layer. Fiber Bragg Grating sensors are a promising technique that might be used to solve this problem. The reduced dimensions of this sensor make it suitable to be inserted directly inside the bondline without significantly influencing the adhesive joint original properties, providing useful information regarding the stress/strain distribution inside the joint.

1.2 Objective

The objective of the present project is to investigate the application of fiber Bragg grating sensors in the experimental determination of the strain distribution inside adhesively bonded single lap joints.

1.3 Methodology

To achieve the aim of this research, the following approach was adopted:

- A preliminary literature review was undertaken, regarding the usage of fiber Bragg grating sensors, single lap joint stress/strain distribution and single lap joint mechanical testing procedures.
- An initial procedure to introduce fiber Bragg grating sensors was used to produce an initial batch of specimens. These specimens used SikaForce®-7888 L10, a high performance polyurethane based adhesive. Simultaneously, single lap joint specimens without fibers were produced.
- Tensile testing was performed on the initial specimens with fibers and without fibers to understand the influence of the fibers in the overall strength of the joint.
- Different procedures to insert the fibers into the joint were evaluated. All the specimens produced by these procedures were tested against the single lap joint without fibers to detect any significant loss of strength and fiber misalignment. The procedure judged to produce the best results was selected to produce the specimens used for the actual strain measuring.
- Single lap joints instrumented with Fiber Bragg Grating sensors were subjected to various loadings in a tensile testing machine. Special acquisition equipment was used to read the strain values measured by the sensors.
- Finite element models of the single lap joint were created in Abaqus® software. 2D and 3D models were simulated to obtain a strain distribution intended to be compared with the experimental results.
- Experimental and numerical values were compared to demonstrate the usefulness of this technique.

1.4 Plan of the thesis

This thesis starts with a literature review of the existing displacement/deformation techniques, comparing their specific capabilities and limitations. In this literature review there is also a section regarding optical fibers and Bragg sensors, explaining in some detail the physical phenomena behind this technology, advantages and limitations, as well as a list of some current applications. Next, a chapter about the experimental details is found, explaining the materials and geometry used, as well as the rationale behind their use. The specimen manufacturing, fiber preparation and mechanical testing procedures are also explained thoroughly in this chapter. Chapter 4 is devoted to finite element analysis. Here, each of the numerical models created for this work is detailed with geometrical information and all the relevant simulation parameters. Chapter 5 features a presentation of the results from all the experimental tests as well as those obtained from numerical simulation work. Comparisons between these results are also made in this chapter. The following chapter, chapter 6, summarizes the main conclusions drawn from the research. This thesis is completed with a chapter including suggestions for future research and further improvements to the procedure.

2. Literature review

2.1 Adhesive bonding: an overview

Adhesive bonding is a relatively recent technology, widely accepted due to its advantageous features comparatively to traditional connection methods, such as bolting, riveting, welding and brazing.

The aerospace industry was the first application area of adhesive bonding, especially from the 1950's. During the following decades, other industries, as shipping and automotive, have been quickly adopting this technology.

Nowadays, adhesive bonding can be found in various places of a vehicle. Although welding is the most common technology used to join metals, the requirements of the automotive industry to reduce the fuel consumption and improve safety for the occupants, revealed some limitations of the spot welding technique in terms of durability and crash resistance. In order to overcome these limitations of spot welding, new technologies have emerged. Structural adhesive bonding is one of these technologies. Whereas the first adhesives employed in the automotive industry did not obtain good results because of their brittle behavior and low resistance to impact loading, new adhesives which combine the high strength of epoxy with the high deformation of typical polyurethane were developed and represent a considerable improvement.

When compared to other traditional methods, adhesive bonding presents a more uniform stress distribution (Figure 1), which allows a greater rigidity and load transfer, improved fatigue strength and vibrations damping. Additionally, adhesive bonding presents an increased ability to join materials with different thermal expansion coefficients and allows the construction of structures with smoother contours (preventing rivets and screws' holes and imprint of welding), a decrease of production's costs and a relatively simple manufacturing process [1].

Adhesive bonding also shows a good strength-to-weight ratio, which allows the decrease of the total weight of structures without any loss of strength.

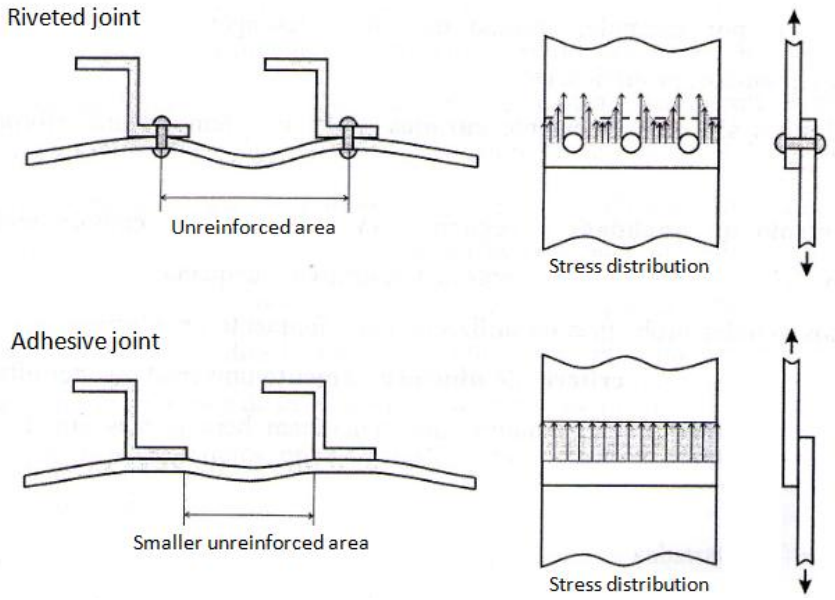

Figure 1- Stress distribution for a riveted joint and for an adhesive joint [1].

To ensure maximum strength, an adhesive joint requires some specific conditions that differ from those used in conventional joining methods. One of the most important conditions is the surface preparation, which must be performed in most cases to ensure that there is not an adhesive failure. Adhesive failures must be avoided at all costs, as they create joints with extremely low strength. Ideally, a joint should exhibit cohesive failure of the adherends, as this creates a situation where the adhesive layer is even stronger than the materials that are bonded. There are various surface preparation methods available and their selection depends on the type of substrates used [1].

Curing times and conditions are also a very important factor to ensure the strength of an adhesive joint. Some types of adhesives and joint geometries require long curing times, specific temperatures or humidity levels that can be hard to implement successfully in industrial or even experimental processes.

Adhesive joints are also very sensitive to environmental conditions. Chemical contamination, extreme temperatures and humidity levels can reduce the strength of a cured joint significantly. Direct sunlight is also very detrimental to the strength of an adhesive joint, as ultraviolet radiation damages the polymeric bonds of the adhesive [1].

The loading direction is also important to ensure a strong adhesive bond. Adhesive layers are relatively fragile in peel, cleavage and impact loadings. Maximum strength is achieved under

shear loading. Adhesive joint geometry therefore must be optimized to ensure that the joint is loaded in the most favorable direction.

The lack of universal failure criteria is also a significant problem when designing adhesive joints. Although there are equations for some joint geometries, the strength of more complex joints is difficult to predict and calculate accurately.

The inexistence of a universal failure criteria coupled with other difficulties in assuring the quality control demonstrate the necessity of using measuring techniques which allow the real-time measurement of physical quantities such as displacement and deformation. This allows the early detection of defects and reduced joint strength, enabling a safer and most consistent performance.

2.2 Overview of displacement/deformation measurement techniques

Understanding and visualizing the deformation field in a structure or component is an extremely helpful tool for designers and engineers. The displacement/deformation measurement techniques allow the identification of critical spots that can be modified and improved, resulting in a stronger and lighter final product.

Over the years, several experimental techniques to measure displacements in a component or experimental specimen were developed. These methods can be divided in two different groups [2]:

- Group I - methods used to measure surface strain;
- Group II - methods used to measure internal strain.

2.2.1 Surface strain measuring methods

The majority of the deformation measurement techniques belong to the first group. Many techniques rely on the surface properties due to practicality reasons, as it is easier to use instruments to register the surface properties.

The superficial strain can be measured through physical phenomena associated to it, such as:

- Variation of the electrical resistance of a metallic thread with axial deformation (electrical strain gauges);

- Phenomenon of occasional birefringence exhibits from some transparent plastic materials when submitted to different states of tension (photoelasticity);
- Crack of brittle coatings applied over the analyzed surface (brittle coatings);
- Optical effect of the formation of fringes which result from the two gratings overlap (Moiré interferometry);
- Interference fringes result from the two holograms or laser speckle field overlap (holographic interferometry and speckle) [3].

A detailed explanation of these surface strain measurement techniques is presented below:

Photoelasticity

The photoelasticity is an optical method for deformation analysis based on a characteristic of some transparent materials whose optical behavior alters with the state of deformation applied to the component. This technique is widely used when the studied structures have complex geometries, are submitted to complex efforts or the analyzed area is large. Photoelasticity allows a global view above the deformation field of a structure.

However, photoelasticity requires the production of a photoelastic model made from a photoelastic material which differs from the analyzed structure (prototype) in terms of dimensional scale and elastic constants of used materials [3].

When the object under study is changed or disturbed in some way, then a pattern of "fringes" will appear on the model, making the object look striped. These fringes really represent maps of the surface displacement caused by the force or stress that disturbed the object (Figure 2).

Figure 2- Pattern of fringes [3].

This displacement map represents an extremely sensitive picture of the actual motion the object has experienced, with a single fringe contour representing lines of equal displacement.

In the case of planar objects, the prototype deformations can be obtained from the model deformations applying the following equation:

$$\varepsilon_p = \varepsilon_m \frac{F_p}{F_m} \frac{h_m}{h_p} \frac{l_m}{l_p} \frac{E_m}{E_p} \qquad 2.1$$

The subscripts *p* and *m* refer to prototype and model, respectively, ε is the deformation, *F* is the load, *h* is the thickness, *l* is a typical dimension in the object plane and *E* is the elasticity modulus [3].

Brittle coating

Another method which can be employed in deformation analysis is the use of brittle coatings. This method consists on the application of a thin layer of a brittle coating over the analyzed surface before applying a load to the surface. Although it is a method whose application is easy and which quickly supplies the location of zones of high stress concentration and the orientation of principal directions, its results are not very accurate. After the coating is dry and while the applied load increases, cracks appears on the surface revealing zones of lower stresses in decreasing order of intensity.

The sensibility of the brittle coating method depends on some features, such as: coating layer's thickness, drying time, application method, and temperature and humidity conditions.

The brittle coating method is a very good auxiliary method of deformation analyzes, mainly in qualitative terms [3].

Moiré interferometry (MI)

The Moiré technique is another deformation analysis method which allows the measurement of a surface's deformation even in the plastic or fluency domain of the material. MI is a purely geometric method which consists in the optical effect of the formation of interference fringes. This interference pattern arises when two gratings are overlaid at an angle, or when they have slightly different mesh sizes (Figure 3).

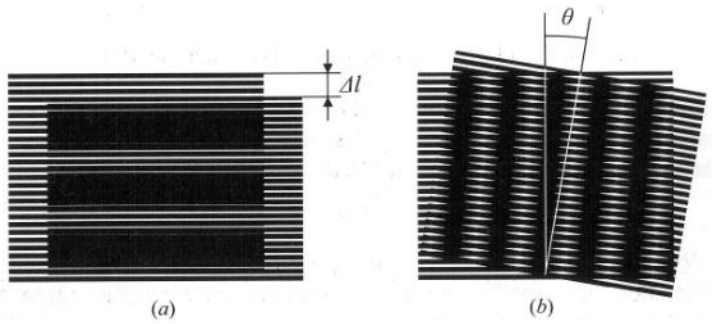

Figure 3- Moiré interferometry fringes. (a)- by deformation and (b)- by rotation [3].

One of the gratings (object grating) is connected to the analyzed surface and the other grating (reference grating) is overlaid to the first one. When the component is deformed or moved, the object grating is deformed or moved too, originating the Moiré interference fringes.

The accuracy of MI depends on the grating's density and on the amplitude of measured deformations [3].

Holographic interferometry and speckle

Holography and speckle are optical techniques of laser interferometry used in deformation analysis whether component is over static or dynamic conditions.

These techniques present some advantages when compared to classic methods of deformation analysis. They are realtime and nondestructive methods which not even need physical contact with the analysed component, do not require a special surface preparation, possess a great sensibility and as photoelasticity supplies a general idea about the distribution of deformation along the analysed surface [3][4].

The optical setup to a hologram recording is schematic in Figure 4.

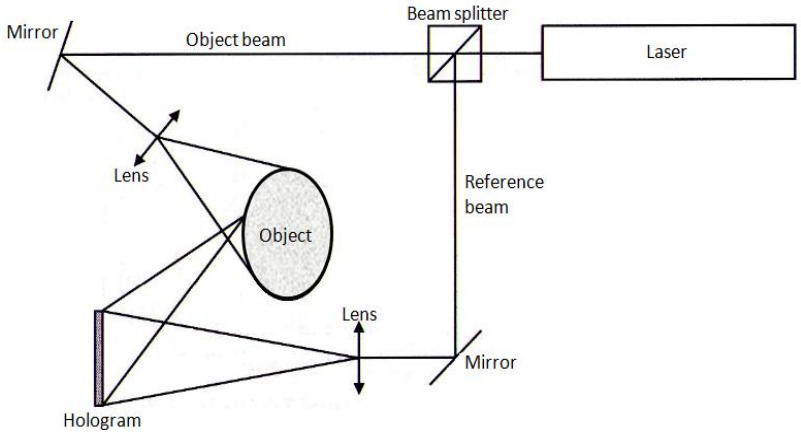

Figure 4- Optical setup to a hologram recording [3].

Holographic interferometry is a technique which enables the analysis of objects with optically rough surfaces and its measurement optical interferometric precision. It is used in vibration and modal analysis, structural analysis, composite-materials and adhesive testing, stress and strain evaluation, and flow, volume/shape, and thermal analysis.

All these applications derive from one or more of the three basic methods of applied holographic interferometry: real-time, multiexposure, and time-average holography [4].

When a rough surface is illuminated by a light beam presents a pattern consisting of light and dark spots (speckle). These spots results from the interference of several light beams derived from the light diffraction on the rough surface. If two speckle fields, each one corresponding to different positions of the analyzed surface, are recorded in the same film and a light beam illuminates the plate, a pattern of fringes appears. These fringes are oriented in the normal direction of the direction of the displacement suffer by the object. The space between fringes is inversely proportional to the amplitude of displacement (Figure 5).

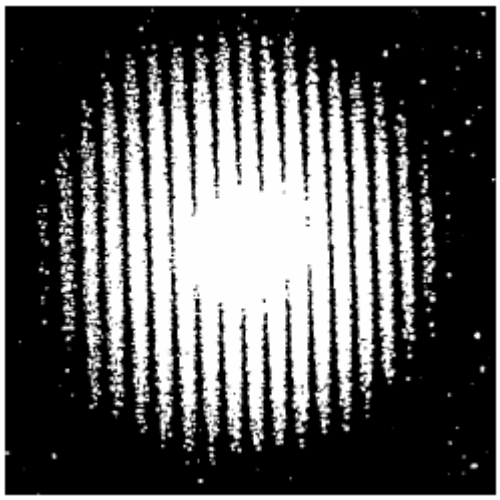

Figure 5- Speckle pattern of fringes [5].

It is important to remember that these techniques only allow the measurement of strain on a surface, not inside the material. There is special interest in understanding the strain inside a material as critical spots are not always located on the surface.

2.2.2 Internal strain measuring methods

There is a limited number of non-destructive methods used to measure the strain inside a solid body. Currently, only two techniques are used for this purpose: Neutron Diffraction (ND) and Bragg grating sensors.

Neutron diffraction is a technique which applies the neutron scattering on the determination of the atomic and/or magnetic structure of a material. Neutron diffraction uses the material's internal crystal structure as a microscopic strain gauge. Although ND is similar to X-ray diffraction, additional information can be obtained using ND because of the different type of radiation used. While X-ray technique uses electromagnetic waves, ND uses particle waves. A sample to be examined is placed in a beam of thermal or cold neutrons to obtain a diffraction pattern that provides information of the structure of the material [6]. Despite the fact of belonging to the restrict group of techniques which allow the measurement of internal strain levels, ND is a technique not often available due to the high technology and costs involved in the generation of neutrons.

Bragg grating sensors are special micro-structures etched inside the core of glass fiber. These sensors act like filters reflecting back a specific wavelength of light. This specific wavelength value can change when the Bragg grating sensor is subjected to an external loading or temperature. By measuring the changes in the reflected wavelength an accurate reading of the strain can be easily obtained. Several of these sensors can be introduced inside a single optical fiber, allowing the simultaneous reading of strain levels in multiple points [7].

As the fibers are sufficiently thin, they can be inserted directly inside the material, such as an adhesive layer or a composite structure. They provide a relatively simple method to be used in the study of strain levels. These unique capabilities led to their use in this work. Bragg grating sensors and optical fibers are discussed in more detail in section 2.4 of this work.

2.2.3 Strain measurement in adhesive layers

In the adhesive area of study, some of these techniques (such as strain gauges and speckle) have been used to measure the adhesive displacement.

The results of da Silva, et al. 2008 [8] show that adhesive deformation can be measured with a simple clip gauge extensometer, however a correction needs to be applied to the measured displacements because the gauge measure the displacement of adhesive+adherends. The adhesive displacements were determined by spacial correlation of image pairs of video microscope.

The spatial correlation method allows to obtain the whole displacement field and it revealed to be a good technique to determined the displacement of the adhesive layer. However, and

due to the required equipment and laborious image processing, spatial correlation is not a suitable technique to be often used. The clip gauge is a very practical and common technique but it requires the use of a correction which can be negligible in the case of flexyble adhesives [8].

Banea, et al. 2009 [9] does not recommend the application of contacting strain measurement techniques (as strain gauging or clip-on mechanical extensometer) in situations where soft elastomeric materials are tested. This fact is because their method of connection and/or weight can influence the final results.

The use of non-contacting strain measurement techniques allows the achievement of the real strain on gauge length of the specimen. In Banea, et al. [9] video microscopy was used to register the adhesive's displacements. Strains were then determined appling the method developed by Chousal and Gomes [9].

The spatial technique is not applicable for thin adhesive layers, as it needs a relatively large surface to measure the displacement of the reference points. In the case of the present work, the thickness of 0.25 mm provides an extremely small area exposed for the imaging. It is very challenging to introduce clear reference points in this area and the camera used to acquire the images must have a very large resolution. This requires lengthy setup times and complex equipment that makes this technique unsuitable for many cases.

Jumbo, et al. 2007 [2] applied neutron diffraction and Moiré interferometry to double lap joints with the objective of quantifying the effects of residual and mechanical stresses alone and combined. Neutron diffraction was also used to measure the total internal strain. There was a good agreement between the results obtained with this methods and finite element simulations [2].

2.3 Optical fiber

Definition and operation principle

An optical fiber is a thin wire of transparent material (glass or polymer) that has the ability to transmit light over a large distance.

The transmission consists of constant reflections (total internal reflection phenomenon) of light on the core's walls, due to the difference in refractive indices between fiber's core and its cladding. The core is always a refractive index higher than the cladding, Figure 6 [10].

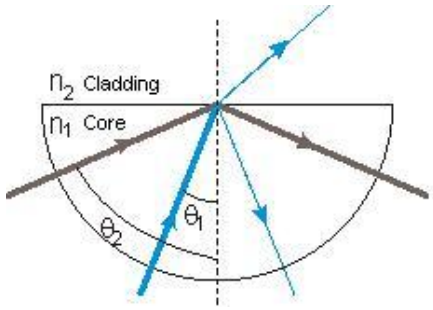

Figure 6- Total internal reflection phenomenon [11].

To ensure the occurrence of the total internal reflection of light phenomenon, another condition must be satisfied: the incident angle has to be equal or greater than the critical angle. The critical angle (θ_c) can be determined by the following expression:

$$\theta_c = arcsin\left(\frac{n_2}{n_1}\right) \qquad 2.2$$

where n_2 is the lowest refractive index and n_1 is the highest refractive index.

- If $\theta < \theta_c$, the light beam will split. Some of the light beam will reflect off the boundary, and some will refract as it passes through;
- If $\theta > \theta_c$, the entire light beam reflects from the boundary. None passes through. This is called total internal reflection [12].

The operation principle of the optical fibers is illustrated in Figure 7, where it is shown the propagation of two independent light signals.

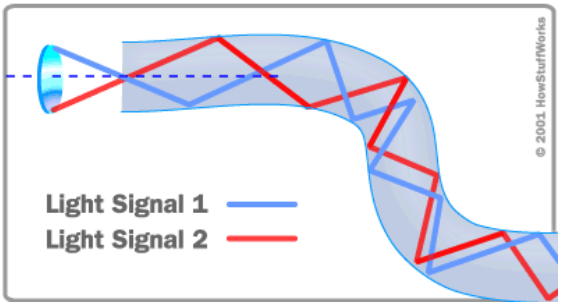

Figure 7- Operation principle of fiber optics [13].

Fiber structure

As illustrated in Figure 8, fiber optic cables are constituted by three basic components:

- The *core* is the thin glass (or polymer) center of the fiber through which the light travels;
- The *cladding* is the outer optical material that surrounds the core and reflects light back into the core;
- The *buffer coating* is a plastic coating that protects the fiber (the core and the cladding) from damage and moisture [14].

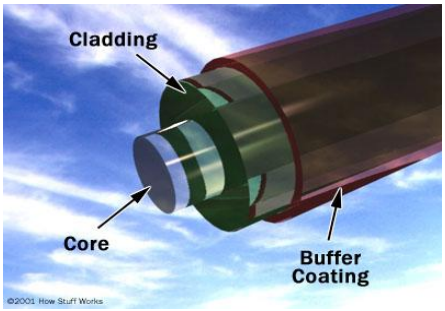

Figure 8- Constitution of fiber optic cable [14].

In the production of the fiber's core, glass is used more often than polymers because it doesn't absorb as much the electromagnetic waves. This glass is made from very pure silica, because the impurities present in the glass causes some signal loss.

Advantages of optical fibers

Due to their features, optical fibers have many advantages over electrical systems, such as:

- Short dimensions;
- Immunity to electromagnetic and radio interferences;
- Very low attenuation;
- Abundant raw material;
- High corrosion and humidity resistance, being usable in wet and harsh environments;
- Lower energy consumption - due to the lower signal attenuation lower-power transmitters can be employed;
- No risk of current leakage or ignition - there is no electricity circulating through the fiber [10-15].

Disadvantages of optical fibers

- Higher keeping costs;
- Fibers fragility when they have no coating;
- Difficult connection between fibers;
- Lack of standardized components [10].

Although slight, a small signal loss (attenuation) is inevitable when light is transmitted through the fiber. This signal attenuation results from the impurities present in the glass and its intensity depends on the glass' purity and transmitted wavelength. Therefore, optical regenerators are attached along the cable to reinforce degraded light signals. An optical regenerator is a length of optical fibers with a special coating (doping). The doped cables allow a laser to be pumped into the fibers, where the doped molecules become exact copies of the incoming lasers. This effectively boosts the strength of the signal and greatly increases the distance the information can travel by fiber optics [14-15].

Applications

Optical fibers are widely used in telecommunications and sensorial systems employed in medicine, automotive and several others industries, such as: military, energy and aerospace.

Advantages and disadvantages of fiber-optic sensors

There is a set of features that make fiber-based sensors appropriate for sophisticated sensing applications. Among these characteristics, minimal signal loss over long distances and high precision optics should be highlighted [16].

Due to these and other advantageous features present by fiber-based sensing instrumentations, there is increasing interest in them.

However, optical sensors have high temperature sensitivity which might be a limitation for certain applications [17].

Physical quantities which can be measured with optical sensors

Optical sensors can be employed for measurement of various physical quantities, such as:

- Displacement (example: monitoring strain levels of a metal bridge structure);
- Temperature (example: study the temperature distribution along a welded joint);
- Pressure (example: monitoring internal pressure of a boiler tank);
- Force and weight (example: high precision scales);
- Acceleration (example: optical accelerometers for hazardous environments);
- Torque (example: monitoring and control of electrical motors) [16].

Methods of attaching the sensors to the structure

There are three methods of attaching the sensors to the structure to be monitored which present potential to be employed in the future:

- Gluing the fiber on the surface of the structure;
- Structural integration;
- Surface integration.

The first method is appropriate for short-term applications; its installation is easy and similar to a strain gauge. The second method is applied to monitor fiber-reinforced materials, being a sophisticated technique. This method presents some disadvantages, like the complex relation between the sensor signal to strain level inside the material and the absence of a technique that allows the insertion and removal of optical fiber in the structure. The relation between the sensor signal to strain level inside the material can be determined in any calibration process of the sensor and represent its sensitivity.

The last technique is a new method where the fiber with sensors is integrated into the coating of the structure. On surface integration, the fiber is part of the surface protection layer. Due to the fiber's high flexibility, it's difficult to handle, so an adhesive tape with holes is used to fix the fiber on the analyzed surface. After fixing the tape with the fiber on the surface, a first layer of paint is sprayed on the tape. The paint that passes through the holes fixes the fiber onto the surface. Then, when the paint is dried, the tape is removed and more layers of paint are sprayed [17].

2.4 Fiber Bragg grating

Definition

A Bragg grating is a small microstructure that may be included in the core of an optical fiber using UV coherent radiation. This microstructure is a located and periodic change in the refractive indice that occurs due to a phenomenon called photosensitivity.

Bragg gratings are sensitive to temperature, axial and transversal deformations, pressure and, in some cases, to a magnetic field [18].

Constitution and fabrication

A periodic modulation of the refractive indice of the fiber core can be introduced using different methods based on pulsed laser irradiation, mainly those by fiber illumination through a periodic phase mask or by a Talbot interferometer. This change can be achieved by introducing activating dopants or by inserting morphologic defects into the fiber core [16].

Phase masks consist on a sequence of longitudinal depressions on the surface of a silica substrat produced by photolithography, Figure 9 [7].

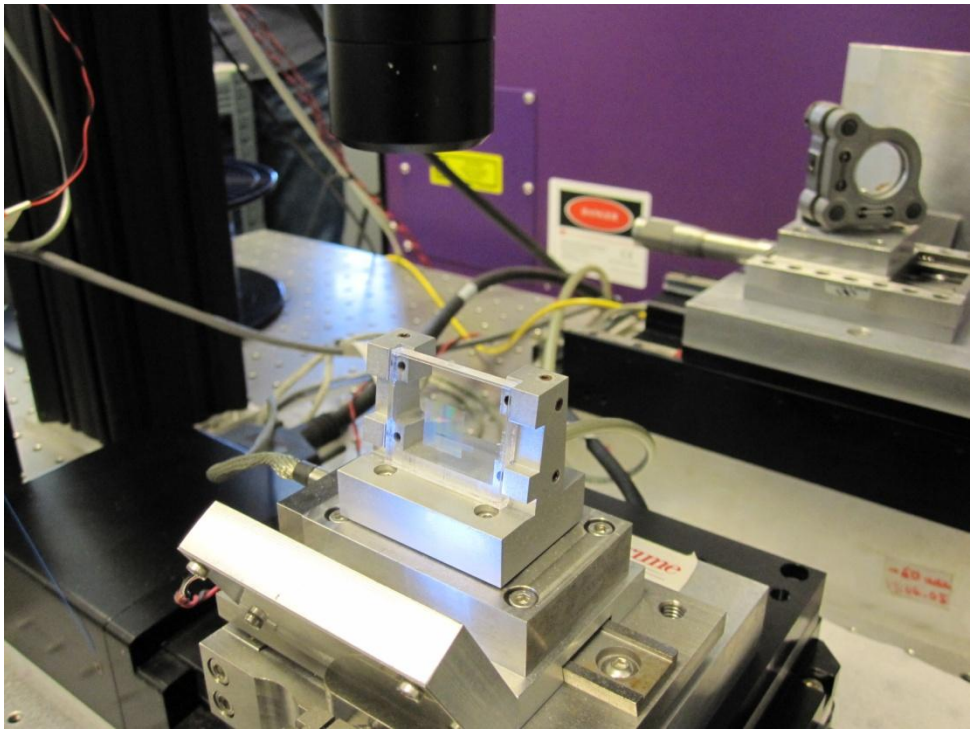

Figure 9- Phase mask - experimental setup of FiberSensing®.

To photo imprint the grating into the core of photosensitive fiber, it is necessary to place the fiber in proximity and parallel to the mask - the phase mask grating grooves are oriented normal to the fiber axis. In Figure 9 can be seen the experimental setup of FiberSensing®. Then the UV laser beam is longitudinally focused on the photosensitive fiber through a cylindrical lens [7].

Figure 10 illustrates the recording of Bragg gratings using the phase mask process. In this method, and considering that this is an ideal phase mask, the diffracted light, which forms a periodic, high-contrast intensity pattern with half the phase mask grating pitch, induces a permanent change in the physical characteristics of the silica matrix. This change consists in a special periodic modulation of the core indice of refraction that creates a resonant structure. In this case, the modulation period of the interference pattern is independent of wavelength of laser emission, just depending on phase mask period. So the fabrication of Bragg gratings with different Bragg wavelengths requires the application of different phase masks [7-19].

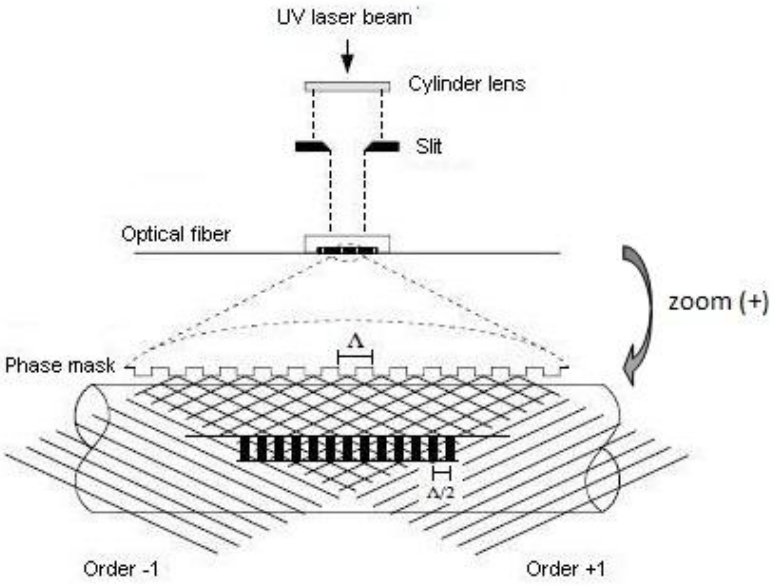

Figure 10- Schematic illustration of the recording of Bragg gratings by the process of phase mask [7].

Operation principle

Since an alteration of the effective refractive index causes a Bragg wavelength deviation, the operation principle of Bragg sensors is based on the measurement of these deviations induced in the resonance condition [7].

Although Bragg sensors are sensitive to various physical quantities, they are mainly used as strain and temperature sensors [7].

Figure 11 illustrates the operation principle of Bragg grating sensors, which can be described simply as: when a light beam from a broadband source is injected in an optical fiber, only light contained in a close range of wavelength centered at the Bragg wavelength is reflected by the grating. The remaining light beam continues its way over the fiber [19].

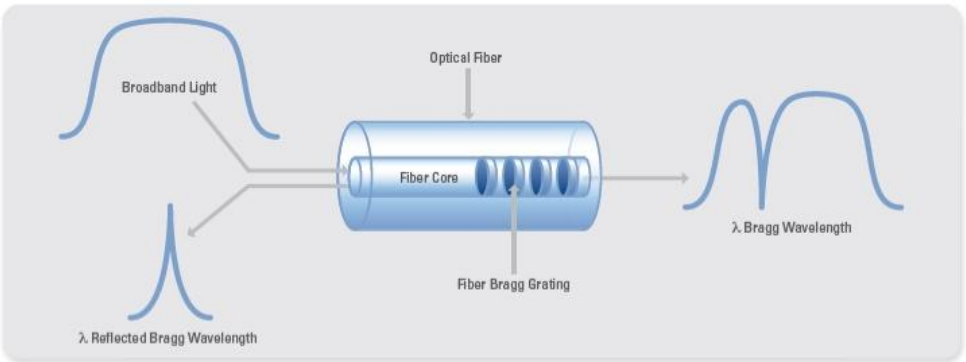

Figure 11- Operation principle of Bragg grating sensors [20].

Bragg wavelength (λ_B) depends on grating period, Λ_B, and effective refractive index n_{eff} of the fiber core.

The effective refraction index is determined by the average between refractive indices n_1 (refractive index of the fiber's core) and n_2 (refractive index of the fiber's cladding) [16].

$$n_{eff} = \frac{n_1 + n_2}{2} \quad 2.3$$

The Bragg wavelength is determined by the following expression:

$$\lambda_B(\varepsilon, T) = 2n_{eff}(\varepsilon, T)\Lambda_B(\varepsilon, T) \quad 2.4$$

Both the effective refractive index and the grating period, and consequently the Bragg wavelength are affected by strain and temperature [16].

Bragg grating acting as a sensor

- Strain sensor

The Bragg grating sensitivity with strain is the simultaneous result of silica matrix physical deformation and effective refraction index alteration due to photoelastic effect [19].

The Bragg resonant wavelength variation with longitudinal deformation is expressed by the equation:

$$\frac{\Delta\lambda_B(\varepsilon, T)}{\lambda_B} = \frac{\Delta(n_{eff}\Lambda_B)}{n_{eff}\Lambda_B} = \left(\frac{1}{\Lambda_B}\frac{\partial\Lambda_B(\varepsilon, T)}{\partial\varepsilon} + \frac{1}{n_{eff}}\frac{\partial n_{eff}(\varepsilon, T)}{\partial\varepsilon}\right)\Delta\varepsilon = (1 + p_e)\Delta\varepsilon = \beta_\varepsilon\Delta\varepsilon \quad 2.5$$

where p_e is the photo-elastic constant of silica and β_ε is the sensitivity to strain [18].

Figure 12 illustrates the effect of tension and compression on a Bragg grating. When the fiber is stretched, the spatial periodicity of Bragg grating increase and, consequently, a wavelength positive variation occurs. On the other hand, a fiber compression causes a decrease in the spatial periodicity of Bragg grating and, consequently, a wavelength negative variation [16].

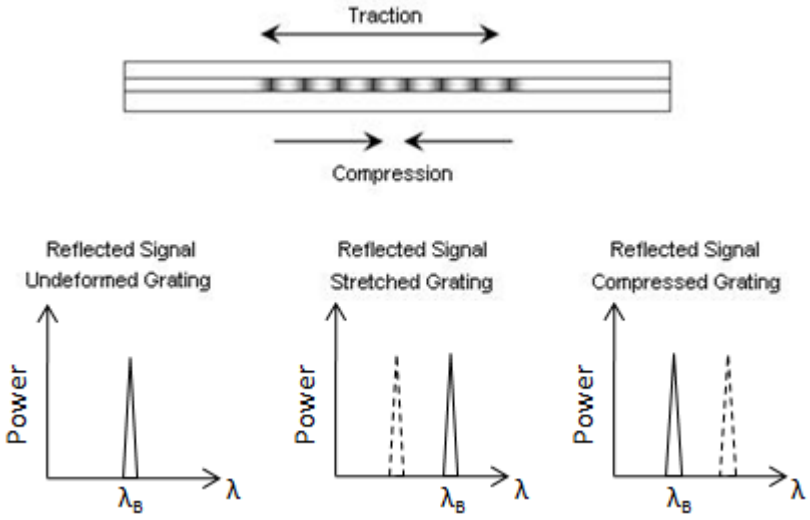

Figure 12- Schematic of spectral displacement of a deformed Bragg grating [21].

- Temperature sensor

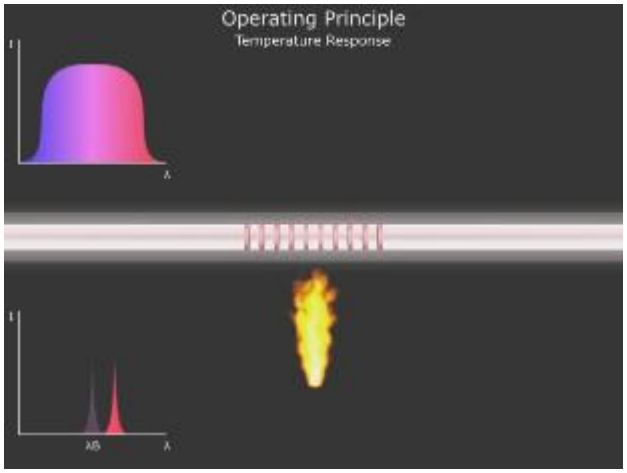

Figure 13- Schematic of spectral displacement of a heated Bragg grating [19].

The Bragg grating sensitivity to temperature is mainly due to the variation of silica refraction index caused by thermo-optic effect. Furthermore, the thermal expansion of the silica matrix, which alters the microstructure period, also contributes to Bragg wavelength alteration [16].

The Bragg resonant wavelength variation with temperature is expressed by the equation:

$$\frac{\Delta\lambda_B(\varepsilon,T)}{\lambda_B}=\frac{\Delta\left(n_{eff}\Lambda_{\mathrm{B}}\right)}{n_{eff}\Lambda_{\mathrm{B}}}=\left(\frac{1}{\Lambda_{\mathrm{B}}}\frac{\partial\Lambda_{\mathrm{B}}(\varepsilon,T)}{\partial T}+\frac{1}{n_{eff}}\frac{\partial n_{eff}(\varepsilon,T)}{\partial T}\right)\Delta T=(\alpha+\zeta)\Delta T=\beta_T\Delta T \qquad 2.6$$

Where α is the coefficient of thermal expansion of fiber, ζ is the thermo-optical coefficient and β_T is the coefficient of thermal sensitivity of Bragg sensor [18].

Advantages of Bragg grating

Being a fiber optic sensor, Bragg grating has all the advantages of optical fibers and fiber-based sensors. In addition, Bragg grating sensors present another advantageous, such as:

- Long-term stability;
- Facility to be integrated into structures;
- High bandwidth fiber optic [17-19].

Additionally, these sensors show two very important characteristics that differentiate them from other optical fiber sensors. Bragg sensors present serial multiplexing and self-referencing capabilities. Multiplexing capability allows the integration of several sensors in a single fiber and their interrogation by a single hardware. Self-referencing capability becomes unnecessary the calibration sensors after the initial calibration [19].

These additional features turn this technology into the most suitable, appropriate and reliable solution for structural health monitoring.

Disadvantages of Bragg grating

Despite all the advantages exhibited by fiber Bragg grating sensors, they present some disadvantages when compared to traditional electrical strain gauges, such as:

- Higher costs;
- Stronger temperature sensitivity;
- Lower strain sensitivity;
- Presence of optical perturbations like birefringence;
- Light loss in the presence of strong fiber bending [16].

Measurements

Bragg grating sensors are available for measuring strain, temperature, acceleration, tilt and downhole pressure and temperature [19].

Applications

There is a set of characteristics that turn Bragg grating into a very important and unavoidable technology for applications in many fields like: civil engineering, aerospace, energy and oil & gas industries, telecommunications (Figure 14), etc.

Figure 14- Application of Bragg grating in telecommunications [22].

With proper packaging each sensor can be made sensitive to parameters different from strain and temperature. Combining multiplexing capability with the ability to measure over long distances, Bragg grating becomes an ideal technology to be employed in all the important phases of structural health monitoring, namely: the construction phase, where the structure parameters can be adjusted in real time; the testing phase, where the response to the loads can be studied to ensure reliability and the long term service, where the installed sensor network allows for constant monitoring during the service life of the structure, Figure 15 [19].

Figure 15- Structural health monitoring using Bragg grating [23].

Furthermore, the small dimensions and weight of the sensors are ideal features for applications where space is restricted and also allows them to be embedded inside composite structures.

In terms of energy industry, Bragg grating became an obvious alternative to electrical strain gauges since they offer greater long term reliability and accuracy of remote measurements.

Here, these sensors are being used to measure strain in overhead lines, to evaluate temperature distribution, to monitor vibration and to map thermally electrical machines.

The immunity to electromagnetic and radio interferences and the inexistent risk of ignition allows the application of this technology in harsh chemical environments as well as in hard-to-reach hazardous locations, typically found in the oil & gas industry [19].

Table 1 contains some examples of Bragg grating applications in several areas already mentioned.

Table 1- Examples of Bragg grating applications

Area	**Examples**
Civil	Structural Health Monitoring during construction, load tests and service life Smart reinforcement of structures
Energy	Temperature monitoring of overhead power lines Temperature mapping in high power generators Hot spot monitoring in high voltage power transformers Vibration monitoring in high power generators Integral blade monitoring system for wind generators
Oil & gas	Monitoring of Pressure and Temperature Down-Hole Detection of low levels of methane Surveillance of pipeline integrity with sensor array
Aerospace	SHM in aircraft fuel tanks Monitoring of in-flight refueling system Temperature monitoring in telecom satellites
Transportation	Automatic weighing and characterization of trains Structural health monitoring of ship hulls
Telecommunication	Production of cables

3. Experimental details

3.1 Materials selected

The adhesive selected is a structural two components and fast curing assembly adhesive, which cures by chemical reaction of its two components.

It is a new adhesive developed and supplied by Sika® Portugal, which is part of a new generation of polyurethane (PU) adhesives that combine the high strength of epoxies and high deformations of elastomers, designated SikaForce®-7888 L10.

SikaForce®-7888 L10 presents several characteristics that make it an attractive product for structural joints where the attainment of rapid strength development and fast cure is an essential requirement. Among these benefits, it can be highlighted the fast strength development and cure at room temperature, the very high strength and elongation and the withstanding high dynamic stresses and bonding well to a wide variety of substrates capabilities.

Apart from its advantageous features, SikaForce®-7888 was chosen because of its higher elongation at break.

The properties of SikaForce®-7888 L10 were obtained from tensile tests performed with bulk specimens. These tests were done by another master student (José Alexandre Neto) and were executed simultaneously with this thesis. From these tests, the stress-strain experimental curves and some mechanical properties of the adhesive were determined (Figure 16 and Table 2).

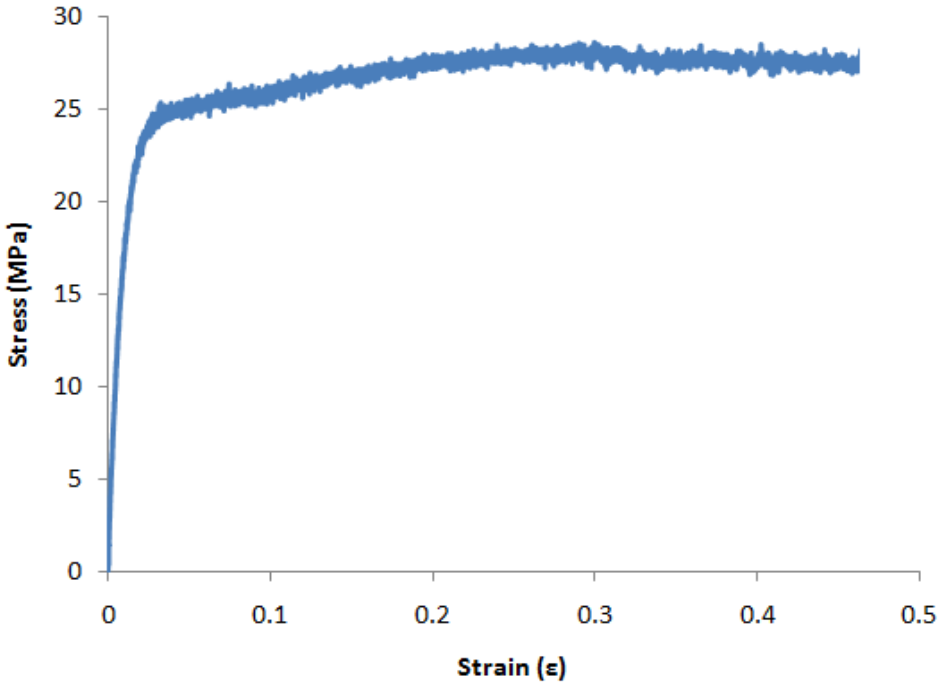

Figure 16- Stress-strain curve of a tested bulk specimen of SikaForce®-7888.

Table 2- Mechanical properties of SikaForce®-7888 L10

Property	Value	Unity
Young's Modulus, E	1.89±0.248	GPa
Yield strength, σ_y	13.20±4.83	MPa
Failure strength, σ_f	28.6±2.0	MPa
Failure strain, ε_f	43±6	%

These properties were used in the finite element analysis presented in a later part of this work.

In order to avoid plastic deformation of the adherends, the substrates were made of DIN C75 steel, quenched and tempered to 44–46 HRC. The tensile properties of adherends are presented in Table 3 [24].

Table 3- Tensile properties of adherend (steel DIN C75) [24]

Young's modulus E (GPa)	Tensile yield strength σ_y (MPa)	Tensile strength σ_r (MPa)	Tensile failure strain ε_f (%)
198.3±11.6	1260±4.5	1413±4.3	20.0±5.1

Two joints using substrates of a unidirectional Carbon Fiber Reinforced Composite (CFRP) with a layup of 16 layers all aligned in the same direction, corresponding to a final thickness of 2.4 mm. The mechanical properties of this CFRP are presented in Table 4.

Table 4- Mechanical properties of CFRP used [25]

Young's modulus (MPa)	Poisson's ratio	Shear Modulus (MPa)
E_1 = 1.09E+05	ν_{12} = 0.342	G_{12} = 4315
E_2 = 8819	ν_{13} = 0.342	G_{13} = 4315
E_3 = 8819	ν_{23} = 0.380	G_{23} = 3200

Direction 1 corresponds to the fiber direction. Direction 2 is the in-plane transverse direction and direction 3 is the out-of-plane transverse direction.

The fibers and sensors used in this project were both supplied by FiberSensing®. The fibers had an external diameter of 0.250 mm and its core's diameter was 0.125 mm. The Bragg sensors etched in the fibers' core had 5 mm of length. Near the sensors and along a distance of 30 mm the fiber' coating was removed, leaving the core visible.

3.2 Specimen geometry

The geometry of the single lap joint specimens used in this thesis is shown in Figure 17. Steel substrates of dimensions 145×25×2 mm^3 were used. The length of overlap was 50 mm and the adhesive thickness was 0.25 mm.

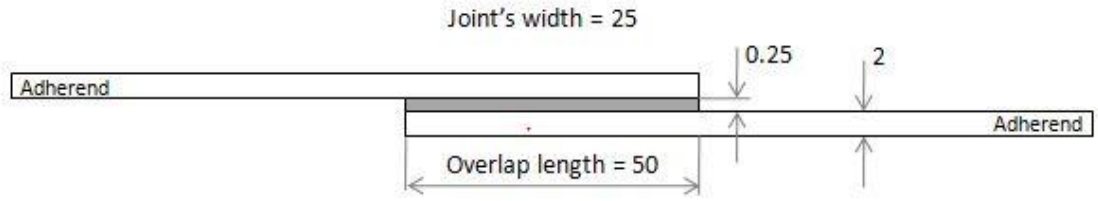

Figure 17- Single lap joint specimen geometry (not to scale, dimensions in mm).

One of the first decisions was the introduction of three fibers into the adhesive layer. Each fiber has a sensor etched and, consequently there are three measurement points. As it is common knowledge, the strain distribution along the overlap length of a single lap joint is not uniform. This effect also exists along the width of the overlap length. The number of sensors

and their positions in the adhesive layer were chosen in order to demonstrate the non uniformity of strain distribution in both directions. Figure 18 shows the positions of fibers (blue broken lines) and Bragg sensors along the adhesive layer.

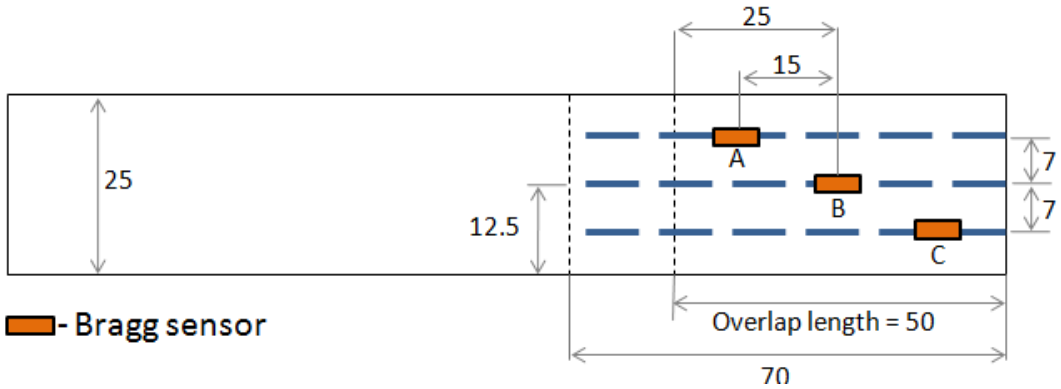

Figure 18- Sensors location in the adhesive layer (not to scale, dimensions in mm).

3.3 Joints manufacturing procedure

In this section the preliminary experimental procedures developed in order to find the best experimental procedure which allows the achievement of the defined objectives are presented.

The steps which compose the joints manufacturing procedure as well as the devices used during this process are described. It is also described the connectorization and polishing processes of the fibers.

3.3.1 Preliminary experimental procedure

The main objective of this project is the determination of the strain distribution in adhesive joints. To achieve this objective it is necessary, in the first place, to measure the displacement suffered by the adhesive joint. For this purpose, Bragg grating sensors are employed. The experimental values will be compared to those resulting from numerical simulation.

After deciding the number of fibers and sensors to be introduced in the joint and their positions, the influence of the presence of fibers on the adhesive joint tensile stress was investigated. Although increasing the number of fibers inserted in the adhesive layer leads to an increase of measuring points, this also results in progressive decrease of the joint strength.

This happens because each fiber inserted in the adhesive layer reduces the bonded area and large number of fibers might cause a significant loss of joint strength.

The greatest difficulty in the joints' production process was to ensure that the fibers embedded in the adhesive layer do not bend during the curing process. This is a fundamental condition, since the orientation of Bragg sensor determines the direction in which the deformation is measured. Several different manufacture techniques were compared, with the objective of determining the most effective at keeping the fibers straight and aligned with the intended direction. During the optimization process optical fibers without sensors were used.

The mould used to produce the adhesive joints is a steel mould constituted mainly by two blocks. In the lower block, alignment pins are introduced to ensure the alignment of joint adherends. The adhesive thickness was controlled by shims (Figure 19 and Figure 20).

All adhesive joints were submitted to a curing time of one day inside the mould, at room temperature, and tested in a MTS servo-hydraulic machine, model 312.31 (Eden Prairie, MN, USA) at a constant crosshead rate of 1.5 mm/min. A load cell of 100 kN was used.

First trial

Firstly, adhesive joints without any fiber were tested in order to know their tensile strength. Simultaneously, joints in which three optical fibers were bonded with cyanocrylate on the extremities of overlap length were produced and tested. In this attempt, spacers were placed in a direction perpendicular to the substrates and distanced from the overlap length limit (Figure 19). As a consequence, a spew fillet was created when the excess of adhesive went out, see Figure 20.

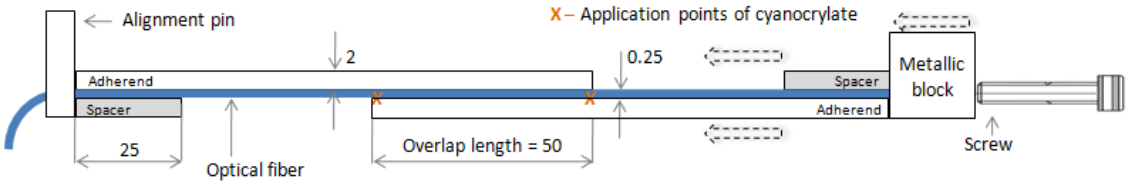

Figure 19- Position of the spacers in the first trial (not to scale, dimensions in mm).

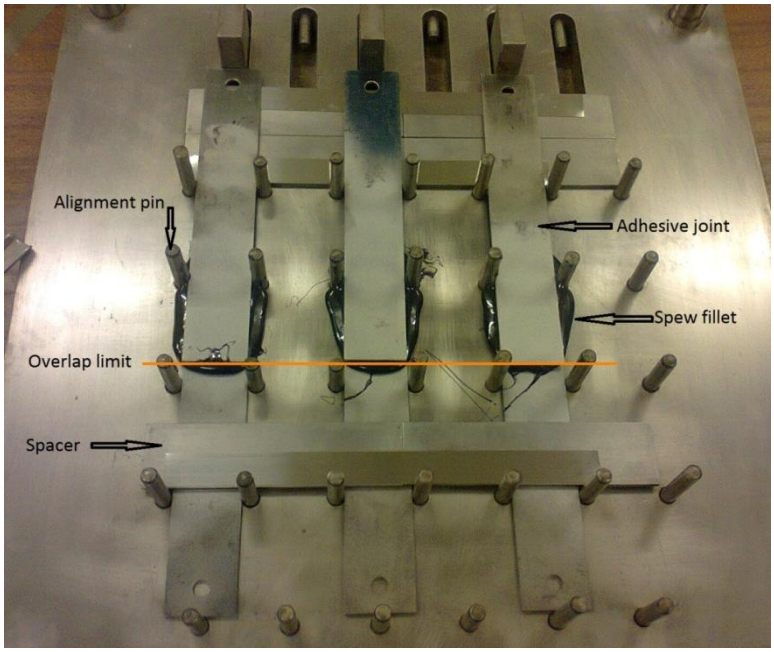

Figure 20- Experimental setup of the first trial.

Figure 21 shows the fracture surface of a joint without any fibers. A cohesive fracture occurred in all three specimens tested and the average of the maximum force registered was, approximately, 30 kN. On the other hand, an interfacial fracture (see Figure 22) occurred in all three joints tested with fibers and the average of failure load was almost half of that obtained for joints without fibers (15 kN).

Figure 21- Fracture surface of a joint without fibers (first trial).

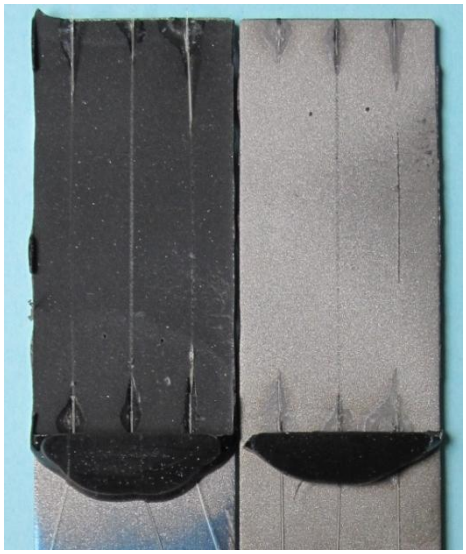

Figure 22- Fracture surface of a joint with fibers (first trial).

One typical load displacement curve obtained from each batch is shown in Figure 23. The great difference in failure load values could originate from the fact that the cyanocrylate acts as an initiator of a crack. However, in this trial, the fibers were straight and linear. In Figure 22 the application of cyanocrylate on the extremities of overlap length is visible.

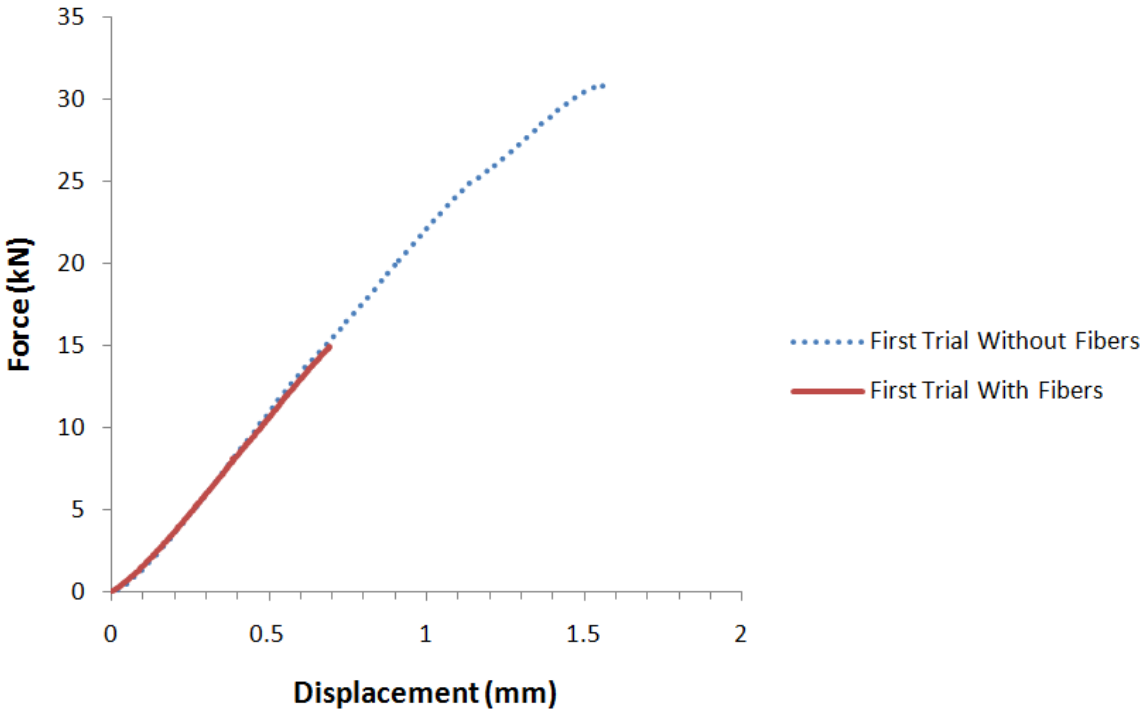

Figure 23- Tensile tests of the first trial.

Second trial

Due to the results of the first trial, it was decided that the cyanocrylate should not be applied along the overlap length. Therefore, in this second trial, one of the extremities of the optical fiber was bonded with cyanocrylate to one of the adherends at 70 mm from the adherend's extremity (Figure 18). The other extremity of fiber was fixed with adhesive tape just outside of overlap length.

In this trial, the spacers had the same orientation as the adherends and as consequence the spew fillet was much smaller than in the first trial (Figure 24).

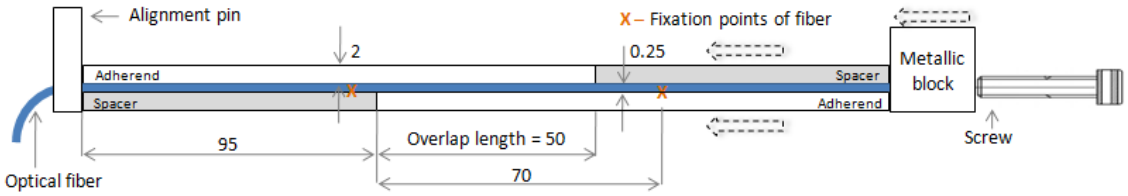

Figure 24- Position of the spacers in the second trial (not to scale, dimensions in mm).

Because of this change in the spacers' orientation, new joints without fibers were produced and tested.

Figure 25 and Figure 26 show the fracture surfaces of the tested specimens. Three joints of each "type" were tested, making a total of six joints. In all specimens a cohesive fracture was identified. In both fracture surfaces, it can be observed that the presence of graphite, used to mark the adherends, introduces zones of adhesive failure. Graphite has a very low surface energy and creates a weak interface between the adherend and the adhesive.

Figure 25- Fracture surface of a joint without fibers (second trial).

Figure 26- Fracture surface of a joint with fibers (second trial).

Figure 26 shows, quite clearly, the misalignment of the optical fibers.

Figure 27 represents one typical load displacement curve, from each batch, of the tested specimens corresponding to this second trial. Since the failure load of joints with and without

fibers is about the same, it can be concluded that the presence of fibers in the adhesive layer does not alter the failure load of the joint. This is a very important fact, because it allows the use of this technology in monitoring of adhesive joints. All six tested joints presented a cohesive fracture.

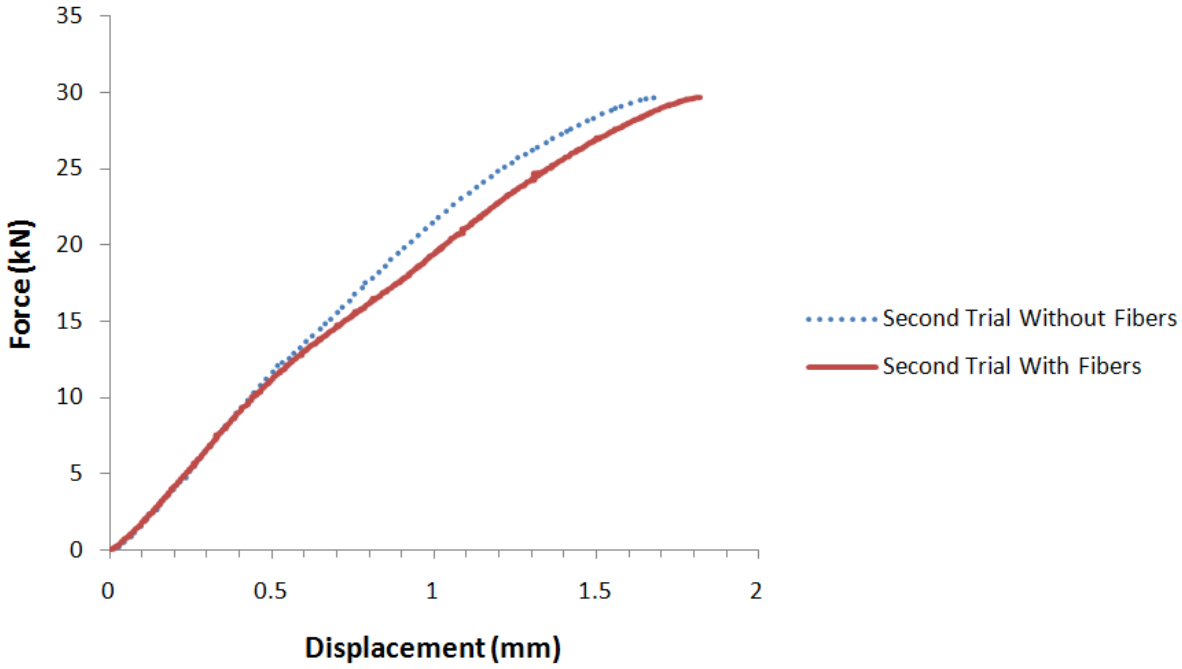

Figure 27- Tensile tests of the second trial.

Third trial

In order to ensure the fibers' alignment, another trial was made. In this attempt, one of the extremities of the optical fiber was bonded with cyanocrylate to one of the adherends at 70 mm from the adherend's extremity and then the fibers were covered with a thin layer of SikaForce®-7888 L10 along the overlap length (Figure 28 and Figure 29) just to fix them to the adherend surface. After a few minutes, when the adhesive cured enough to hold the fibers in place, the remaining adhesive was applied and the upper adherend placed.

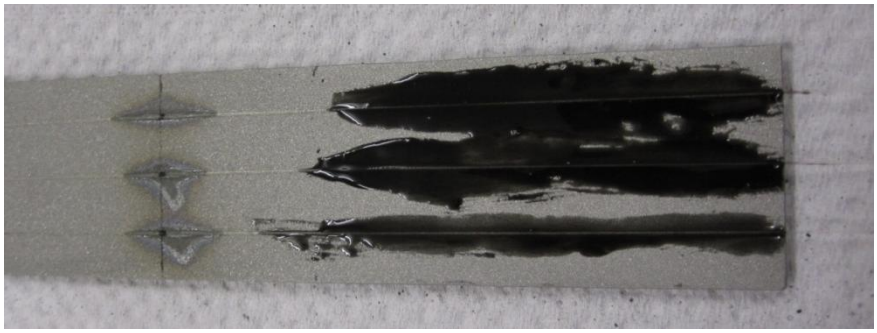

Figure 28- Adherend with fibers covered by a thin layer of SikaForce®-7888 L10.

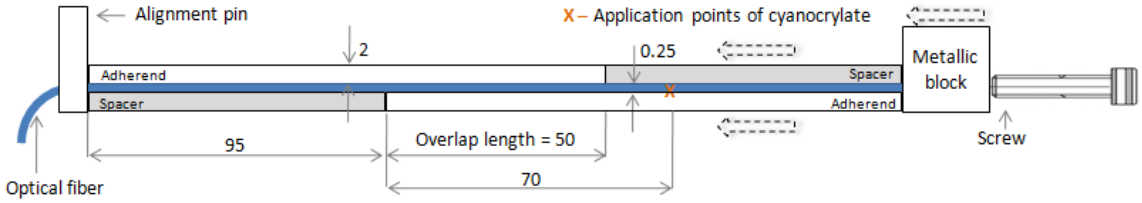

Figure 29- Schematic representation of the experimental setup of the third trial (not to scale, dimensions in mm)

Figure 30 illustrates a fracture surface of a joint of this third trial. It can be observed that the lateral fibers were not linear. A cohesive fracture occurred in all three tested joints.

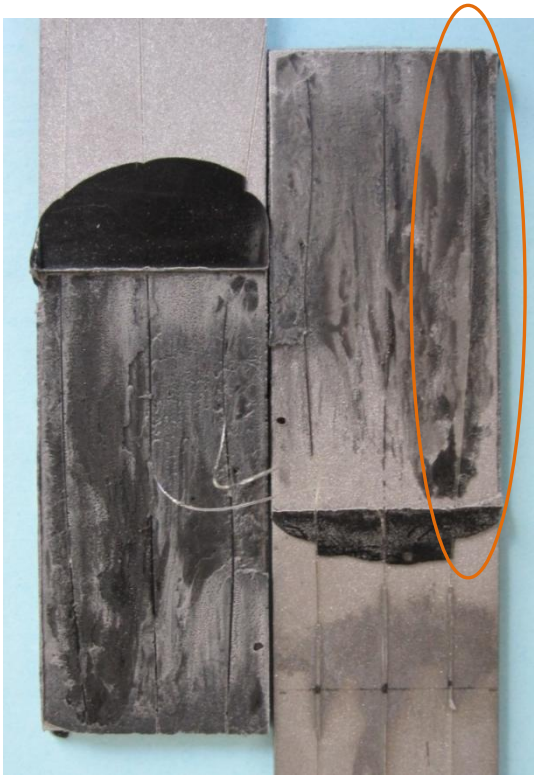

Figure 30- Fracture surface of a joint (third trial).

Figure 31 represents the force *vs* displacement curves of the third trial's tested specimens. As can be observed, the results of the three joints were very scattered. When the "second layer" of adhesive is placed, it is applied over the preliminary layer that already initiated its curing process. The surface tensions involved in this connection are very close and results in insufficient surface wettability. This fact is a possible reason for this results' dispersion and the decrease in the joints' failure load. For an easier and better comparison a load *vs* displacement curve of a joint without fibers is included in Figure 31.

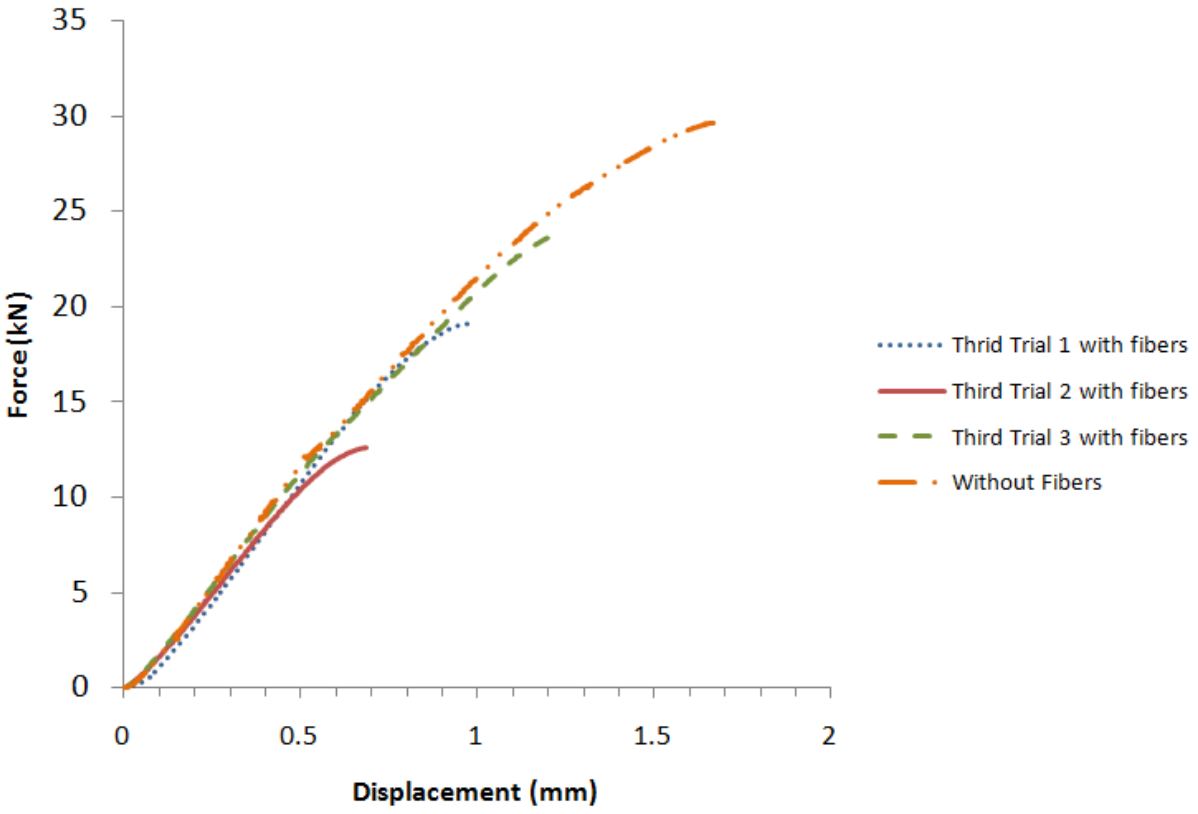

Figure 31- Tensile tests of the third trial.

Fourth trial

In this fourth trial, the process of bonding fibers to the adherends was changed. One of the extremities of the optical fiber was bonded with cyanocrylate to one of the adherends at a distance of 70 mm from the adherend's extremity. The other extremity of fiber was bonded to the opposite adherend, in the same conditions (Figure 32).

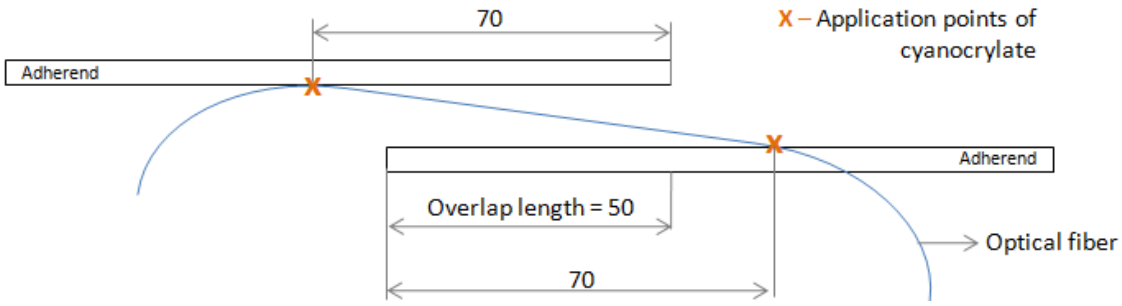

Figure 32- Fiber bonded to adherends in the fourth trial (not to scale, dimensions in mm).

Another modification introduced was the heating of adherends before the application of the adhesive. For this a heat gun, whose designation is Black & Decker KX2000K, was used (Figure 33).

Figure 33- Black & Decker KX2000K.

When the adhesive is applied on a heated adherend there is an increase of its fluidity, which facilitates the flow of excess adhesive between the fibers.

Figure 34- Fracture surface of a joint (fourth trial).

Figure 35- Fracture surface of another joint (fourth trial).

Figure 34 and Figure 35 represent two fracture surfaces of the joints produced by this fourth trial. As can be observed, this process does not ensure the alignment of the fibers. This happens due to the dimensional tolerances of mechanical elements involved (spacers and adherends) which allow the existence of a slack space between these elements (Figure 36).

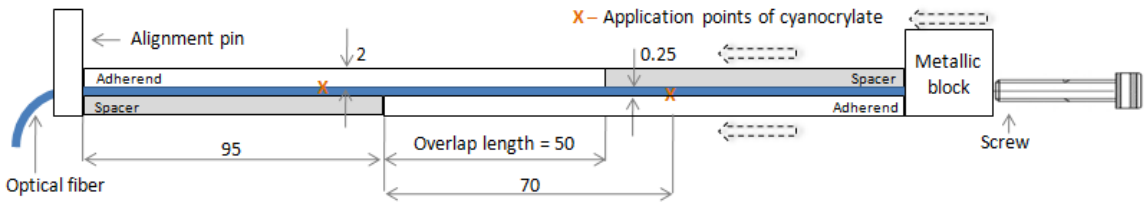

Figure 36- Schematic representation of the experimental setup of the fourth trial (not to scale, dimensions in mm).

During the cure process a small contraction of the adhesive occurs and, consequently, fibers bend because they are not fixed to a surface along the overlap length, but just in two points out of overlap length (Figure 32). This fact exposes the necessity of applying a constant tension to the fibers, before and during the cure process, preventing them from bending under the force exerted by the adhesive and keeping them linear. Therefore, an auxiliary mechanism or a new experimental process is required.

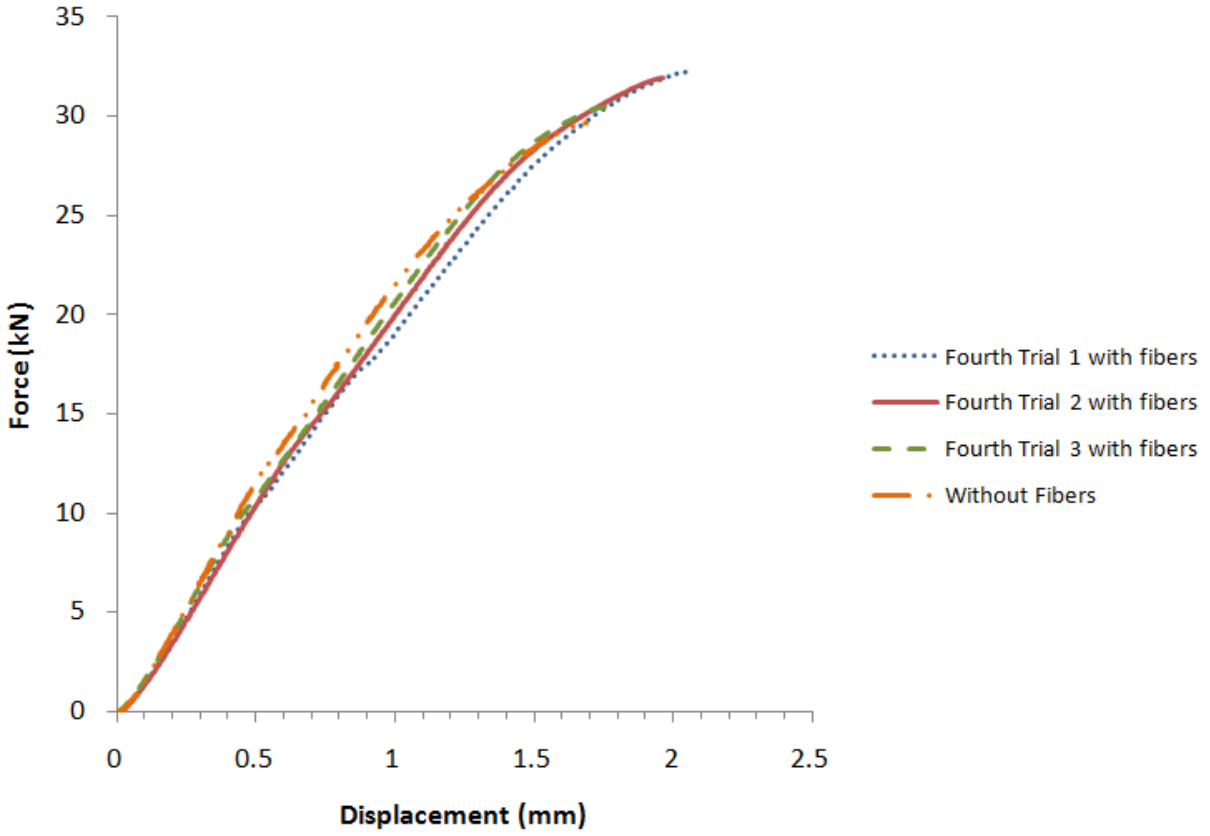

Figure 37- Tensile tests of the fourth trial.

Figure 37 illustrates the load displacement curves of all three joints produced by the method described in the fourth trial. As can be concluded, the force *vs* displacement curves of these joints are similar to those previously exhibited and the average of tensile stress is near to 31500 N. For an easier and better comparison a load *vs* displacement curve of a joint without fibers is included in Figure 37.

Fifth trial

In order to apply a constant tension to the fibers, a small change in the experimental process was introduced. This modification is based on the utilization of longer spacers (Figure 38).

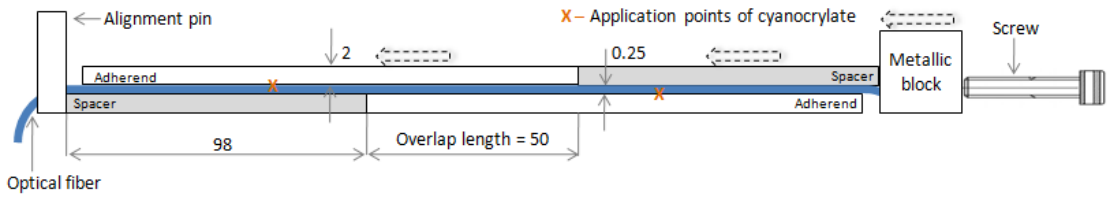

Figure 38- Schematic representation of the experimental setup of the fifth trial (not to scale, dimensions in mm).

After the positioning of the upper adherend and spacer, a metal block is translated with the aid of a screw and, consequently, the upper spacer and adherend slide, moving away from the lower adherend and stretching the fibers.

The fibers were bonded to the adherends as illustrated in Figure 32. As in the fourth trial, the adherends were also heated, in order to increase the adhesive's fluidity and, consequently, improve the fibers' alignment.

Figure 39 shows a fracture surface of one specimen produced by the fifth trial procedure. A cohesive fracture, near the surface, occurred in all tested joints. In this figure an improvement of fibers' alignment is visible.

Figure 39- Fracture surface of one specimen of the fifth trial.

In terms of tensile tests, the behavior of these joints is similar to those tested in the fourth trial. Six joints were produced and tested. Figure 40 shows the load displacement curves of three of these joints. For an easier and better comparison a load *vs* displacement curve of a joint without fibers is included in Figure 40.

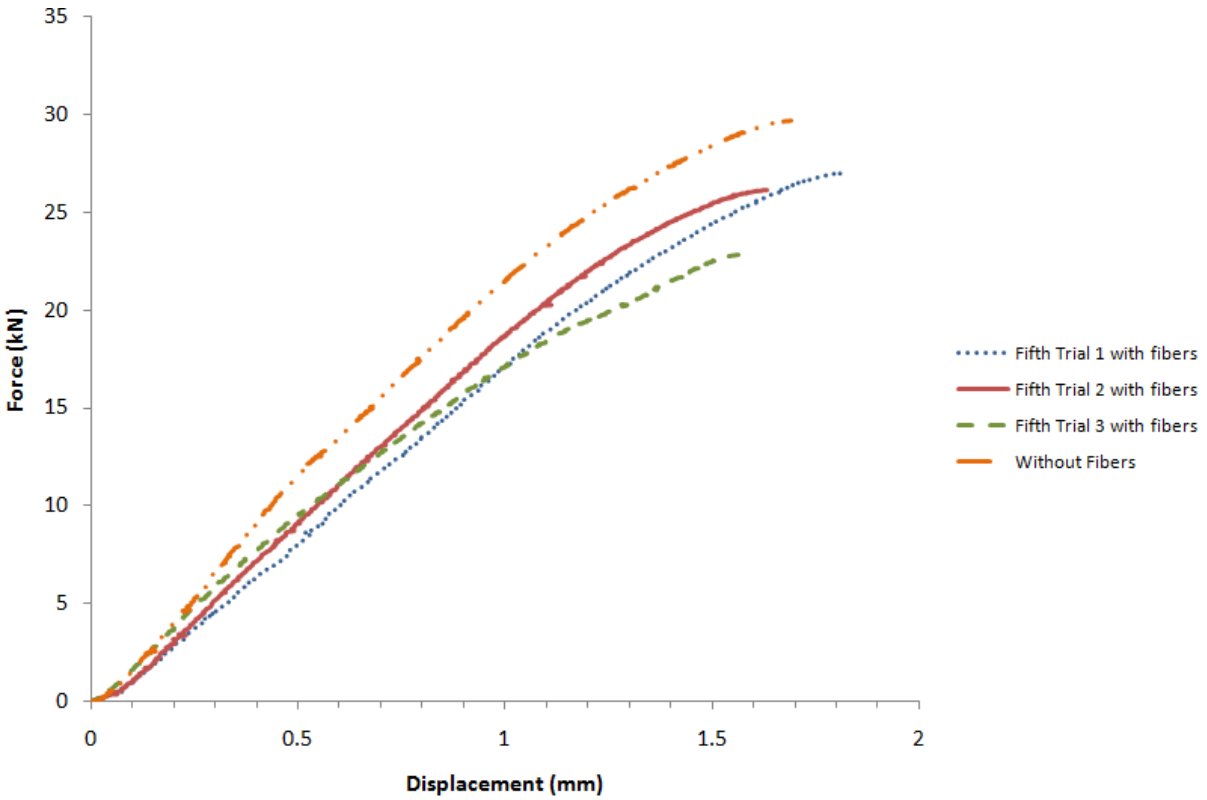

Figure 40- Tensile tests of three joints of the fifth trial.

The procedure described as the fifth trial was the one adopted to produce joints with fibers and Bragg grating sensors. The other steps of experimental procedure are now described in detail.

3.3.2 Complete joint manufacturing procedure

The experimental procedure starts with the cleaning of the steel mould with acetone to remove all grease and impurities present. Release agent, Loctite® Frekote 770-NC, is then applied on the mould surface to prevent that the adhesive bonds to this surface. After these steps, the mould is prepared to receive the adhesive joints.

The metallic adherends are sandblasted to prepare their surfaces, followed by a cleaning with acetone. The adherends are then marked to identify the points where the fibers are bonded to adherends' surface and the limit of overlap length (Figure 18).

After that, fibers are bonded to the adherends' surfaces, the adherends and spacers are positioned on the steel mould and pre-heated to a temperature around 100°C (Figure 41).

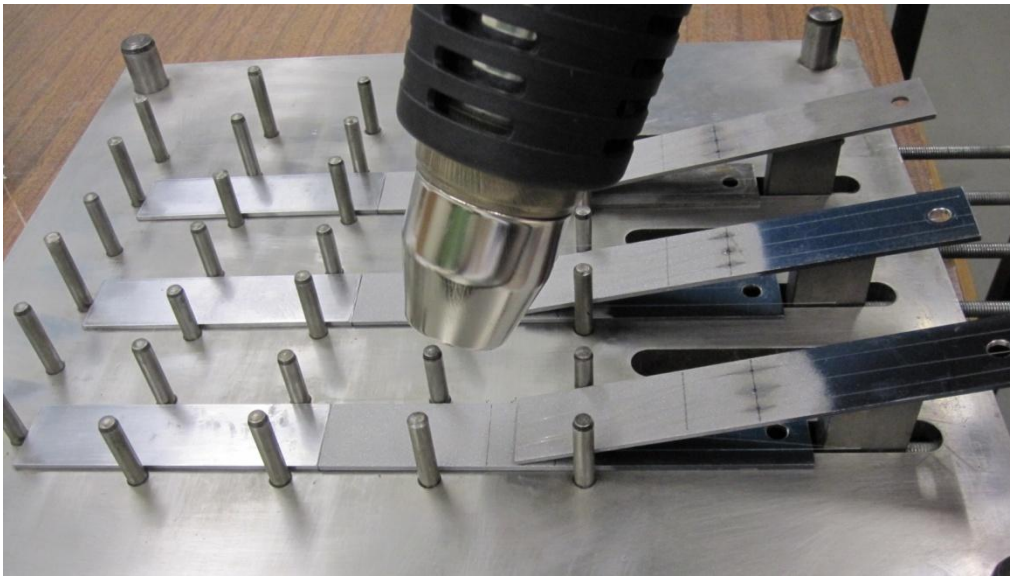

Figure 41- Positioning and pre-heating of metallic adherends.

A Fluke Ti25 infrared camera was used to control and record the adherends temperature, Figure 42 and Figure 43.

Figure 42- FLUKE Ti25 infrared camera.

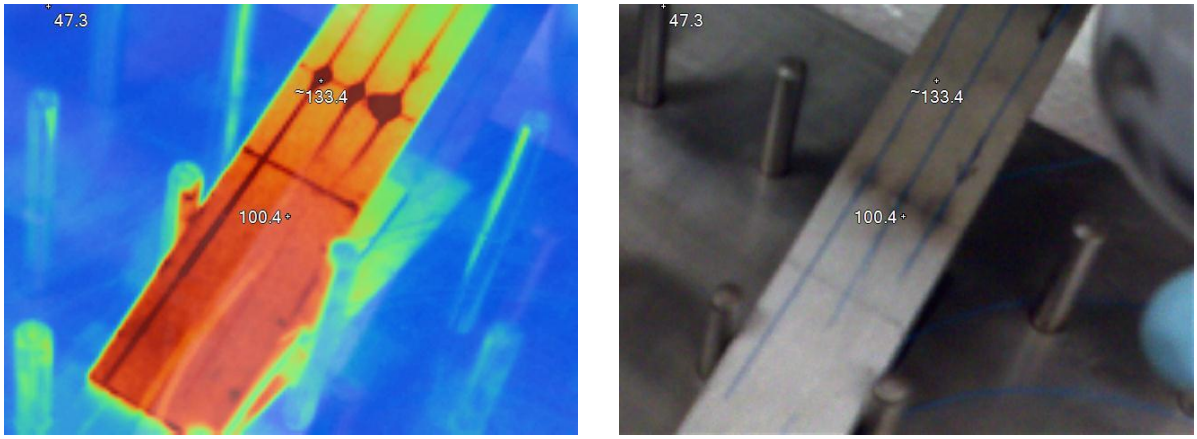

(a) (b)

Figure 43- Thermographic camera images. (a)- Infra-red image. (b)- Real image.

A small portion of adhesive is poured into a plastic recipient using an adhesive applicator gun (Figure 44).

Figure 44- Adhesive's extraction using an adhesive applicator gun.

The two parts of the adhesive are then mixed, during two minutes at a speed of 1500 rpm, in a SpeedMixer DAC 150.1 FVZ-K (Figure 45) to obtain a homogenous mixture.

Figure 45- SpeedMixer DAC 150.1 FVZ-K.

While the adhesive is being mixed, the adherends are heated, before the application of the adhesive.

After the mixing is completed, the application of the adhesive must be quick because the cure process of SikaForce®7888-L10 occurs in a few minutes.

Figure 46- Adhesive's application.

After adhesive application, the upper adherend is placed in the correct position (Figure 47). The other spacer is then placed between the upper adherend and the metallic block and the adjusting screw is used to introduce a higher and constant tension to the fibers (Figure 38).

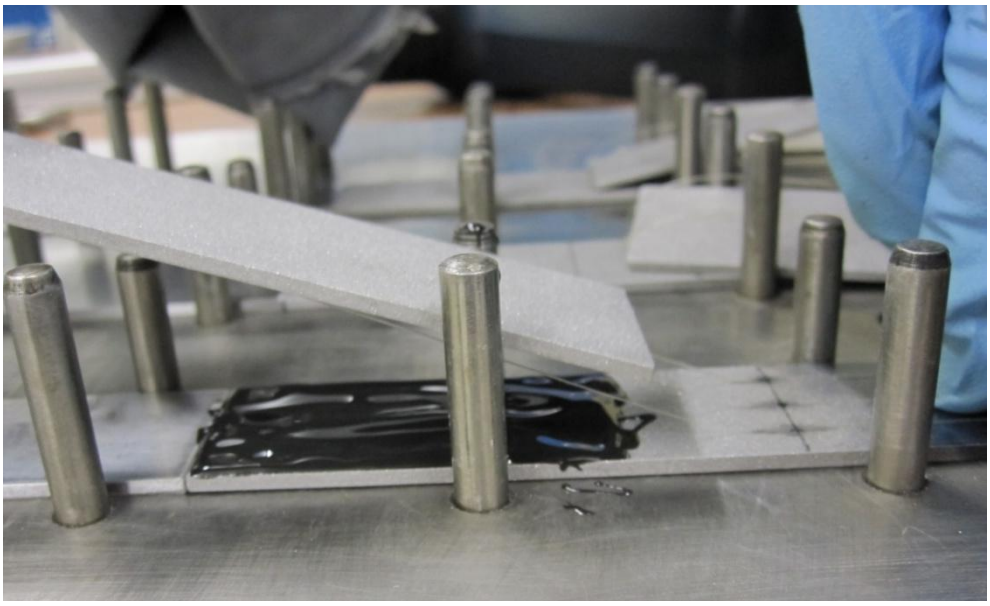

Figure 47- Positioning of the upper adherend.

To ensure that the adhesive layer is completely full of adhesive, pressure is applied on the upper adherend until excess of adhesive appears around all the overlap area (Figure 48).

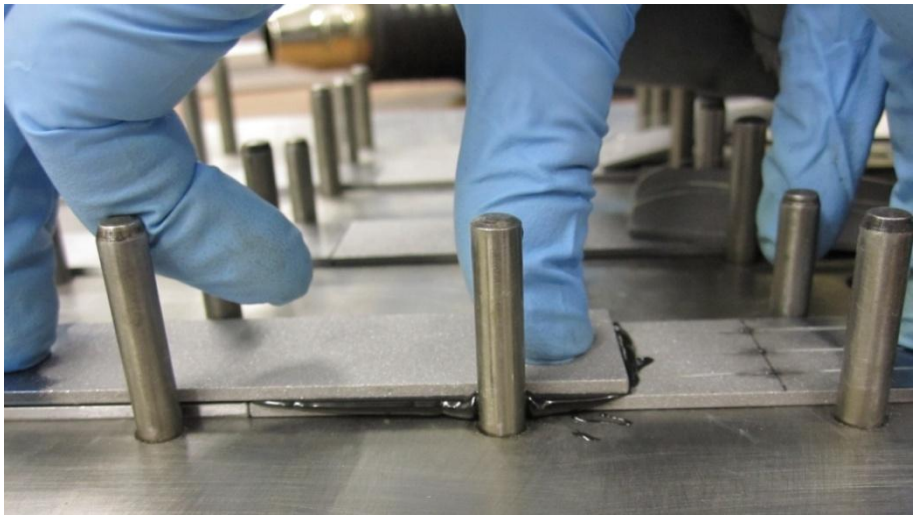

Figure 48- Appling pressure on the upper adherend.

After all the joints are manufactured, the steel mould is closed and a constant pressure is applied to all joints (Figure 49).

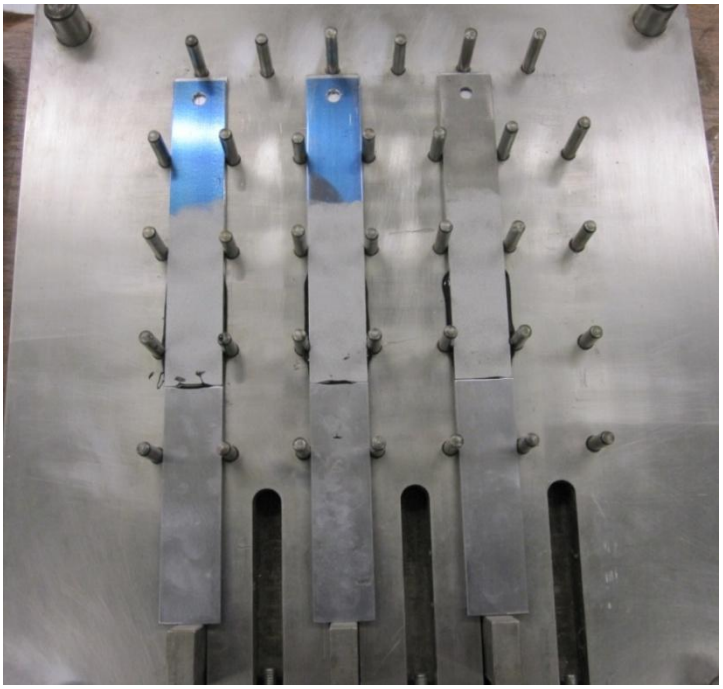

Figure 49- Mould with joints immediately before closing.

After the joints' produced process optimization is concluded, it was time to produce joints with fiber where Bragg grating sensors are recorded. However, before the joints' production, it is necessary to prepare the fibers to be used in the joints. This preparation process is divided in two main parts: fiber connectorization and polishing.

3.4 Fiber Bragg preparation

In this section of the thesis the experimental procedure related with the connectorization and polishing of fibers are described. The measurement unit used during the experimental tests is also presented.

3.4.1 Fiber connectorization

The connectorization process of the optical fibers requires the application of several standard and fiber/connector specific tools. In the next paragraphs the principal steps which compose this process are summarize and presented the tools and components used.

The fiber connectorization begins with the slipping of a strain relief boot and a crimp sleeve onto the end of the fiber (Figure 50).

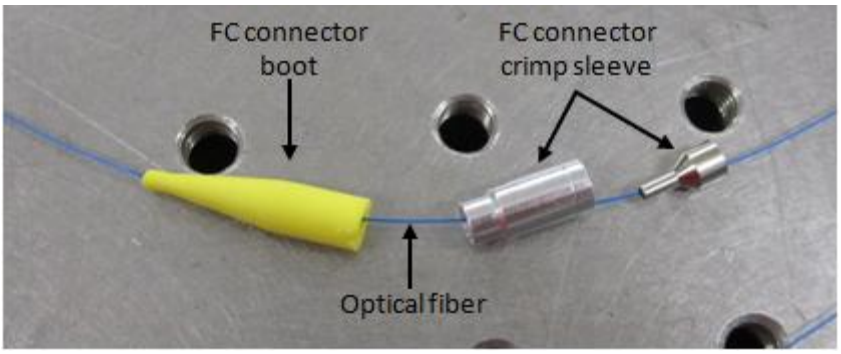

Figure 50- FC connector boot and crimp sleeve into the optical fiber.

Afterwards, the same extremity of the fiber is stripped using a stripping tool (Figure 51).

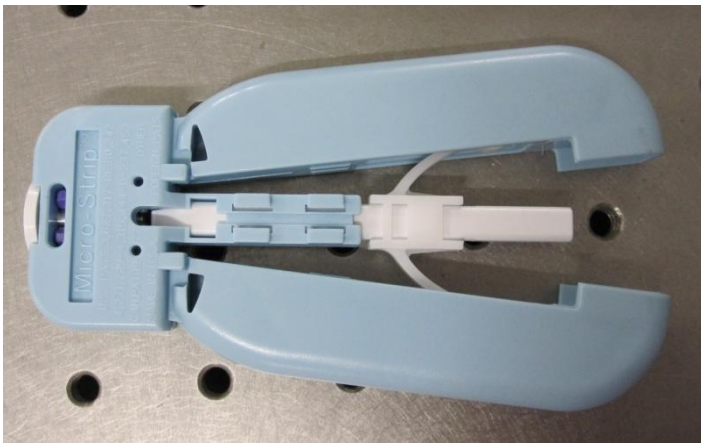

Figure 51- Fiber stripping tool.

The stripped extremity is then clean with reagent-grade isopropyl alcohol. All remaining particles of fiber's cladding and other debris must be removed from fiber.

When the fiber is clean and dry, the fiber and connector are tested. It must be ensure that fiber fits into the connector and the length of exposed fiber is enough for connectorization. If this condition is not verified, the connector should be removed from the extremity of fiber and the length of stripped section should be adjusted. In this step, the optical fiber and connector should be tested without any epoxy [26].

It follows the preparation of epoxy used to bond the fiber to the connector. The curing schedule of epoxy used in this procedure is presented in Table 5.

Table 5- Epoxy curing Schedule [26]

Designation	Pot Life	Cure Time at 25 °C	Typical Cure Schedule	Operating Temperature	Cured Color
F112	40 Minutes	18 Hours	15 Minutes at 65 °C	-60 to 110 °C	Blue

As the epoxy employed is a two parts epoxy, these two components have to be mixed until a homogenous mixing is obtained. The mixing is then poured into a syringe (Figure 52).

Figure 52- Epoxy is poured into the syringe.

In the next step, the syringe is inserted into the back of the connector. While maintain a constant pressure between the connector and the syringe tip, the syringe's plunger is pressured and the epoxy is injected into the connector until a small bead appears on the outside face of the connector ferrule (Figure 53) [26].

Figure 53- Add epoxy to the connector.

When the hole's connector is full of epoxy, the stripped section of fiber is carefully inserted into the epoxied connector. The crimp sleeve is then placed over, pressured against the back end of the connector and crimped using the crimp tool (Figure 54) [26].

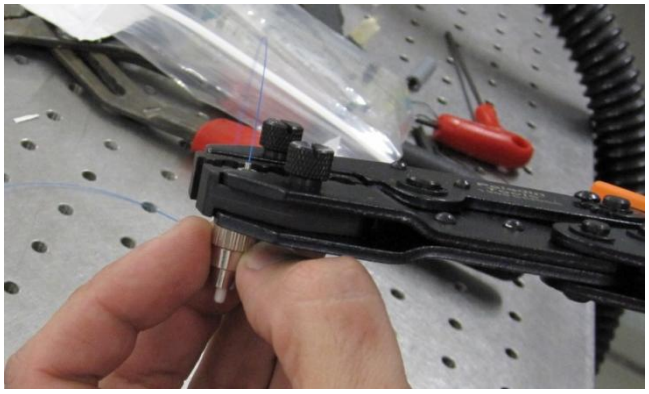

Figure 54- Fixing the crimp sleeve with the crimp tool.

After that, a small amount of epoxy is added where the crimp sleeve meets the fiber (Figure 55).

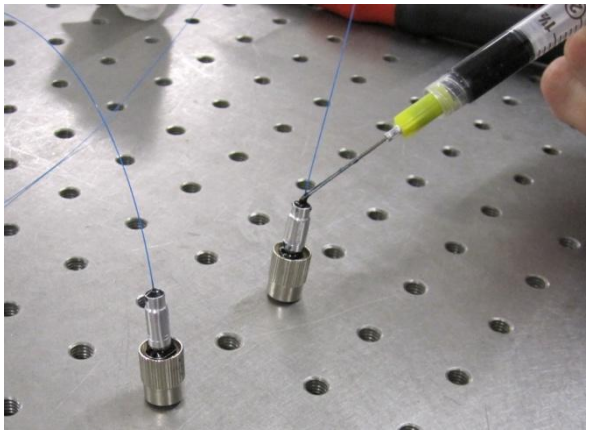

Figure 55- Add epoxy to the crimp sleeve.

The epoxy used has a curing time of 18 hours. The curing process must be very slowly to avoid large volume contractions, which could inserted bending efforts in the fiber and, consequently break it, mainly in the stripped sections.

3.4.2 Fiber polishing

When the fiber is connectotized and, to provide a low signal loss connection, the exposed fiber at the connector must be cleaved and polished.

The polish process begins with the scoring of the fiber. Using a fiber scribe, the fiber is lightly scored just above the epoxy bead. The cutting edge of the scribe must be perpendicular to the salient fiber (Figure 56).

Figure 56- Scoring the optical fiber.

Before starting the normal polishing procedure, the protruding fiber must be hand polished using a polishing film of 5 μm and rubbing the fiber in a back and forth motion. Repeat this motion until the fiber is flush with the epoxy bead [26].

Now and after cleaning the glass polishing plate, clear the rubber polishing pat and place it over the glass plate.

After cleaning the bottom surface of the polishing disc, insert the connector into the polishing disc and start the normal polishing procedure. Using a film of 5 μm and without applying downward pressure, begin polishing the fiber in a figure of eight pattern.

As the fiber and epoxy bead are polished, pressure between the connector and the polishing film can be gradually increase.

When a thin film of epoxy remains on the ferrule tip, the 5 μm polishing film and disc can be cleaned with isopropyl alcohol to remove all debris and substituted by a 3 μm polishing film. The connector should be polished, also in a figure of eight pattern, until a faint hint of epoxy remains on the connector end. Repeat the procedure for polishing films of 1 μm and 0.3 μm (Figure 57) [26].

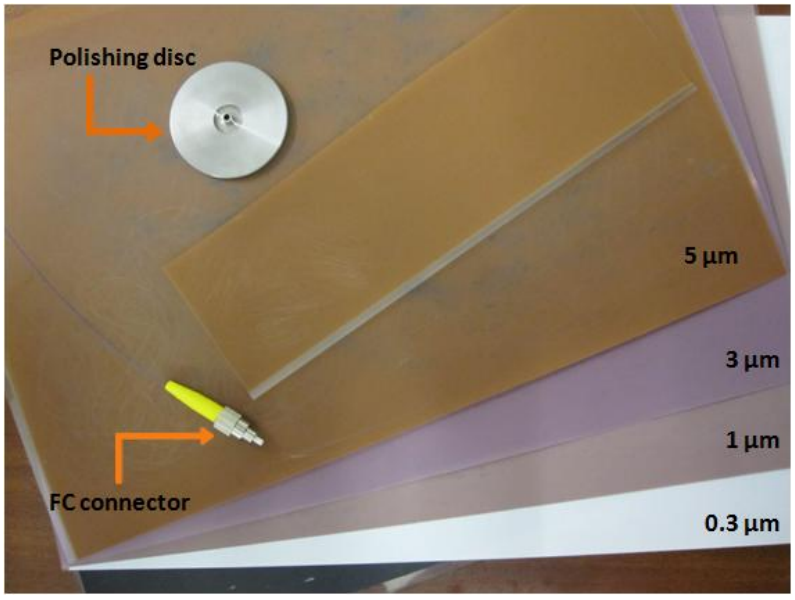

Figure 57- Polishing disc, FC connector and polishing films used.

After finishing the polishing procedure, the connector end surface must be clean with isopropyl alcohol and analyzed using a 200X inspection microscope (Figure 58), to ensure that it is free of debris and epoxy.

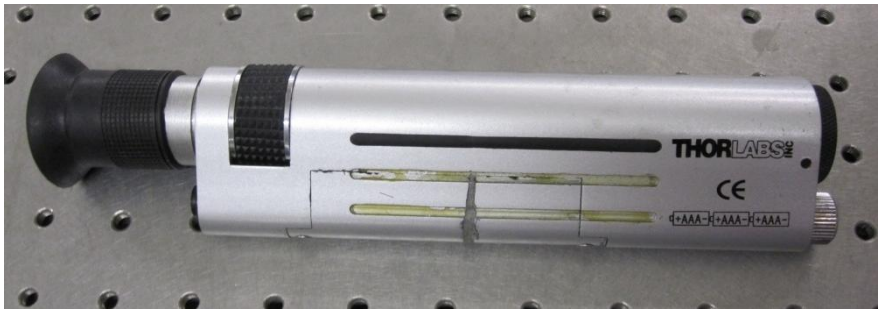

Figure 58- Fiber inspection scope CL-200.

The fiber must be flush with the end connector surface and the core of the fiber does not contain heavy scratches as illustrated in Figure 59 [26].

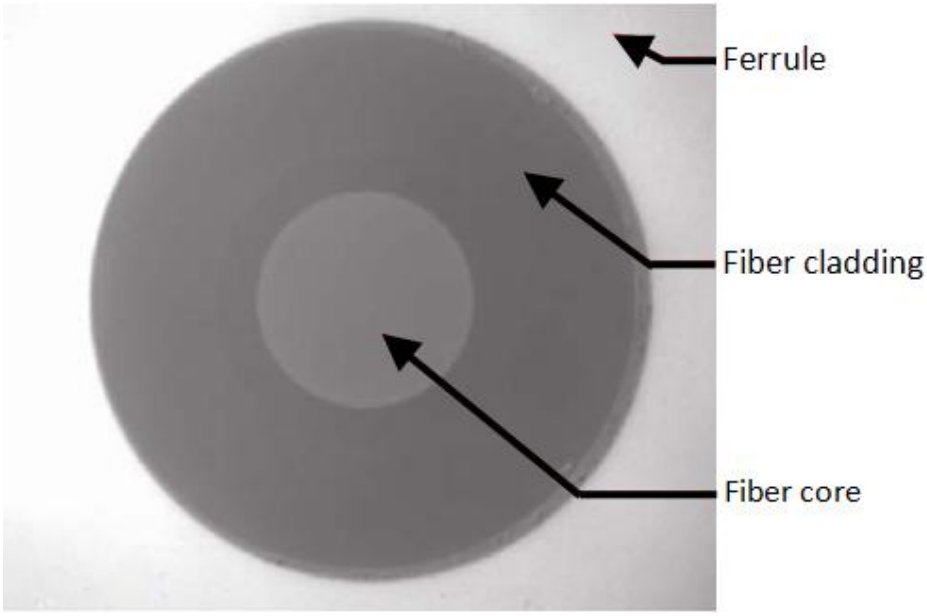

Figure 59- Well polished fiber connector [26].

If the connector does not pass in final inspection, repeat the polish with polish films of 1 μm and 0.3 μm.

For a more detailed description consult the "Guide to Connectorization and Polishing Optical Fibers" available in Thorlabs® website.

As the described processes of fiber connection and polishing require substantial time and accuracy, it was decided to purchase/acquire special equipment which dispenses these

processes. Universal bare fiber terminators and FC connectors were acquired from Thorlabs® company (Figure 60).

Figure 60- Universal bare fiber terminator and FC connector.

3.4.3 Measurement device

The measurement device used during the experimental tests was kindly supplied by FiberSensing®. This FiberSensing industrial BraggMETER FS2100 | FS2200 measurement unit is designed and produced to interrogate fiber Bragg gratings sensors in industrial environments and measure the absolute Bragg wavelength in real-time.

Figure 61- BraggMETER FS2100 | FS2200 measurement unit.

4. Finite element modelling

A numerical simulation of the tensile tests was made using the software Abaqus/CAE 6.10-1.

The main objective of this simulation is to determine the strain distribution in the joint. It is also desired to compare the results of this simulation with the experimental values, since it was not possible to determine these values using another experimental technique. As explained before, the majority of the deformation measurement techniques are just available to measure superficial strain and, on the other hand, even those currently applied to adhesive joints exhibit limitations when the adhesive layer is too thin. Due to these reasons, a finite element analysis was then chosen as a reference method, as it allows the determination of the deformation inside the adhesive layer.

To these purposes, plastic analyses were performed.

For a first estimate of the strain distribution inside the adhesive layer, a two dimensional (2D) plastic analysis is sufficient. However, it is also necessary to execute a three dimensional (3D) analysis in order to extract the strain distribution in various points along the adhesive joint width.

Firstly, a 2D deformable shell with the shape of the adhesive joints produced was modelled.

4.1 2D analysis

Data

The adhesive properties, as well as, the steel properties introduced to the numerical analysis were previous presented in “Experimental details” section. For both materials a Poisson’s ratio of 0.33 was considered. Figure 62 shows the numerical curve used in the plastic numerical analysis developed.

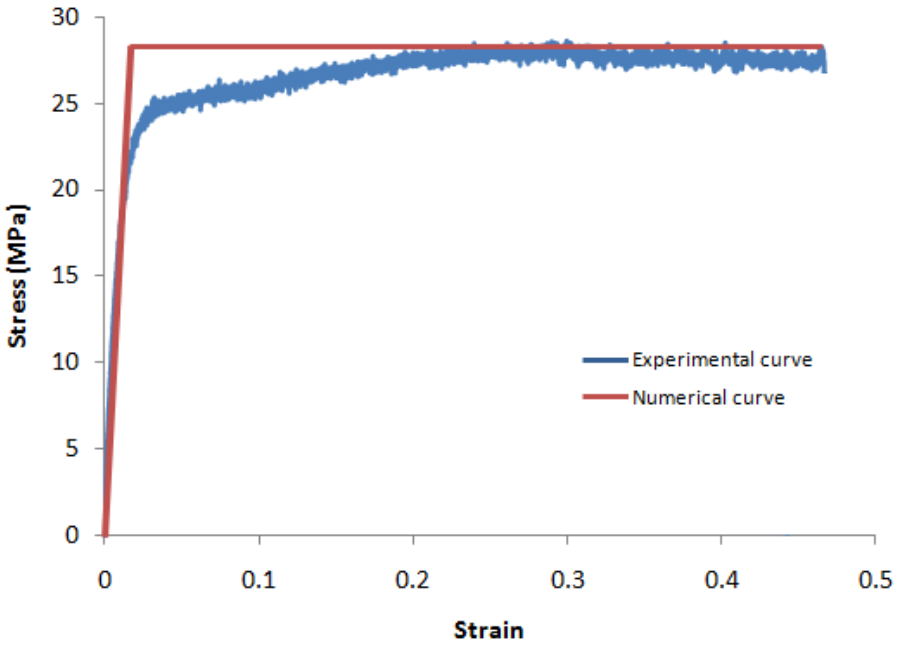

Figure 62- Numerical curve considered.

Boundary conditions

Since one of the objectives of this simulation is to compare its results with the values obtained from experimental tensile tests, the boundary conditions applied must be as similar as possible to the real experimental conditions (Figure 63).

Figure 63- Boundary conditions of the finite element model (not to scale, dimensions in mm).

As illustrated in Figure 63 one of the ends of the specimens was fixed with an encastre and on the other end a load of 5 kN was applied. This value corresponds to the maximum load applied to the joints during the experimental tensile tests. Movement along the yy axis was also restricted in two 25 mm long sections, near both ends of the specimen. This boundary condition simulates the clamps of the MTS machine (Figure 64).

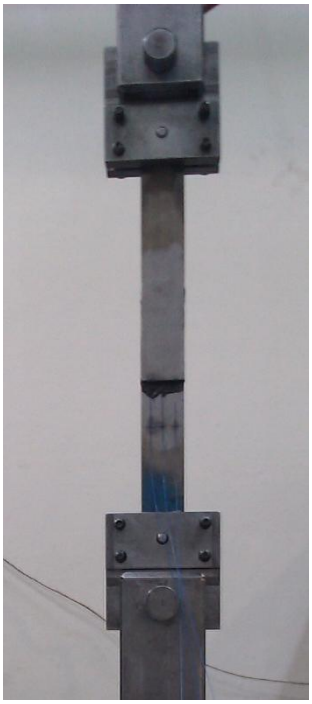

Figure 64- Adhesive joint assembled to MTS machine.

Mesh

The mesh established was formed by CPE4R elements which are 4-node bilinear plane strain quadrilateral elements with reduced the integration, making the calculation faster [27].

Initially, a general mesh composed by elements with 0.250 mm of length was generated. However, this initial mesh contained too many elements and it did not allow a good understanding of the strain distribution in critical zones. To improve the strain distribution study, a mesh optimization procedure was executed applying local seed edges. This was done in order to obtain a more refined mesh along the overlap length and in the adhesive layer (Figure 65). Additionally, a coarser mesh (composed by elements with 1 mm of length) was applied on the extremities of the joint, along a length of 75 mm. As the analysis is focused in the strain distribution along the overlap length, the joint's extremities zones are not critical areas.

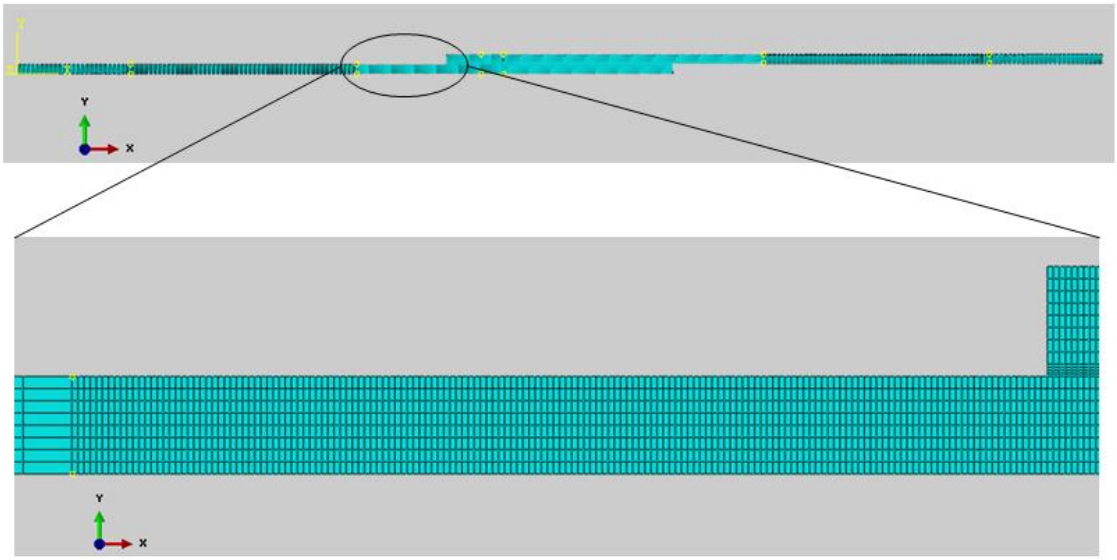

Figure 65- Finite element mesh of the overlap area.

The mesh on the joint's extremities was kept constant. In the overlap zone, different local meshes were tested in order to identify the mesh which provides better results with less complexity. The length of elements was changed just in the "x" direction. The attributed values to this dimension and the total number of elements and nodes are indicated in Table 6.

Table 6- Length of elements in the "x" direction along the overlap area (dimensions in mm).

Length of elements in "x" direction	**0.100**	**0.125**	**0.200**	**0.250**
Total number of elements	14400	11760	7800	6480
Total number of nodes	15471	12651	8421	7011

To study the suitability of the different meshes, the von Mises stress distribution along the overlap was analyzed (Figure 66). A von Mises stress distribution was chosen because includes the influence of all the stress components.

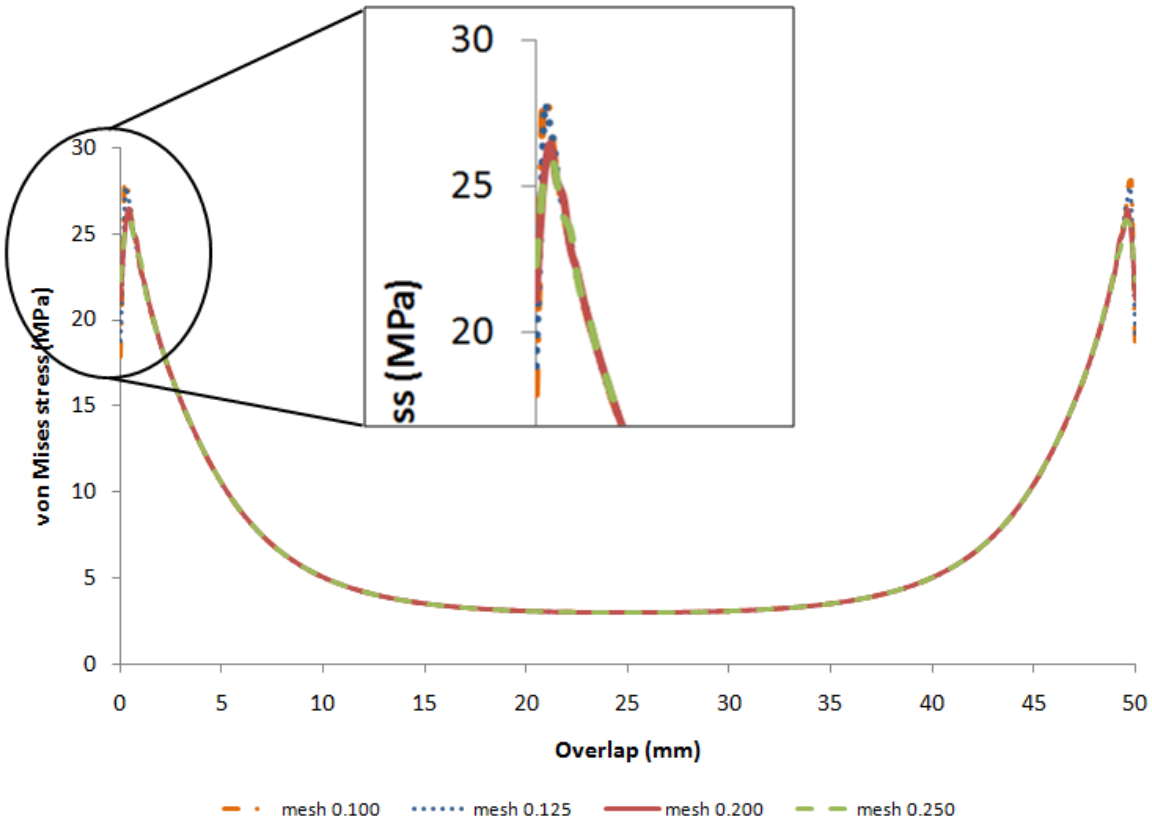

Figure 66- von Mises stress distribution for different meshes of an applied load of 5 kN.

Figure 66 shows that all four meshes tested present the same behavior along the overlap length, except on the extremities. On the extremities, just the more refined meshes (mesh 0.100 and mesh 0.125) can reach higher stress values, better representing the real stress distribution along the overlap length. As it can be observed, the difference between the two refined meshes is not significant, then and according to the data presented in Table 6, the mesh 0.125 seems to be the one which presents the best results without increasing excessively the total number of elements and nodes. Due to these facts the mesh 0.125 was selected to be used in the 2D analysis. In the overlap area, the selected mesh was formed by 8000 elements and 11370 nodes.

As mentioned before, the strain distribution along the overlap length of a single lap joint as well as along the width of overlap length is not uniform. This fact must be taken into account when finite element results are compared with experimental results. A 2D model, as presented above, is useful for understanding the joint strain distribution along the overlap length, but to understand the strain distribution along the overlap width, a 3D model is required.

4.2 3D analysis

A 3D deformable solid was created by extrusion of the profile geometry of the adhesive joints produced (adherends and adhesive layer).

The data inserted was the same of the 2D simulation.

Boundary conditions

In order to reduce the complexity and time required for the calculation just an half of the specimen (12.5 mm of width) was modelled in this 3D analysis. As a consequence, an additional symmetry boundary condition was introduced.

Mesh

The mesh was formed by C3D8R elements which are 8-node linear brick 3D stress elements that reduced the integration [27].

Along the overlap length (direction "x") local seeds with the same length of the mesh used in the 2D analysis (0.125 mm) were created. In the overlap width direction local seeds with 1 mm of length were used to create the mesh (Figure 67).

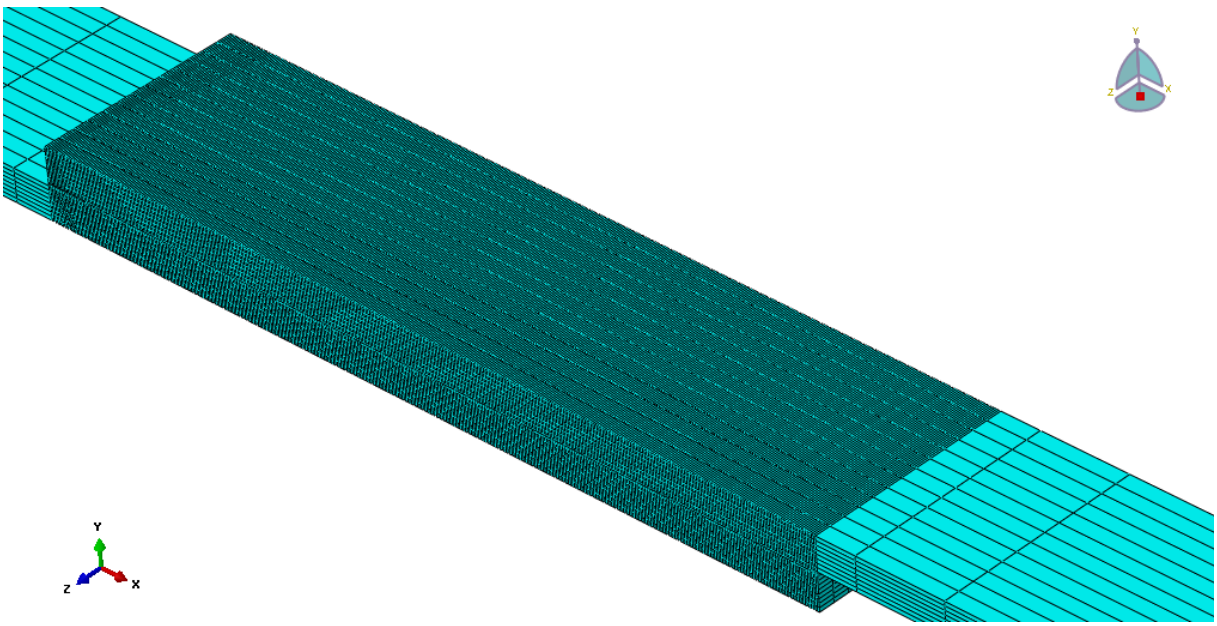

Figure 67- Finite element mesh of overlap area.

Local seeds were also created along the adherends length in order to obtain a more refined mesh near the overlap area and simultaneously to reduce the total number of elements. In this

case single bias was applied (Figure 68). Due to the complexity of this type of 3D mesh, it is very important to optimize the element number, as this can greatly reduce calculation times.

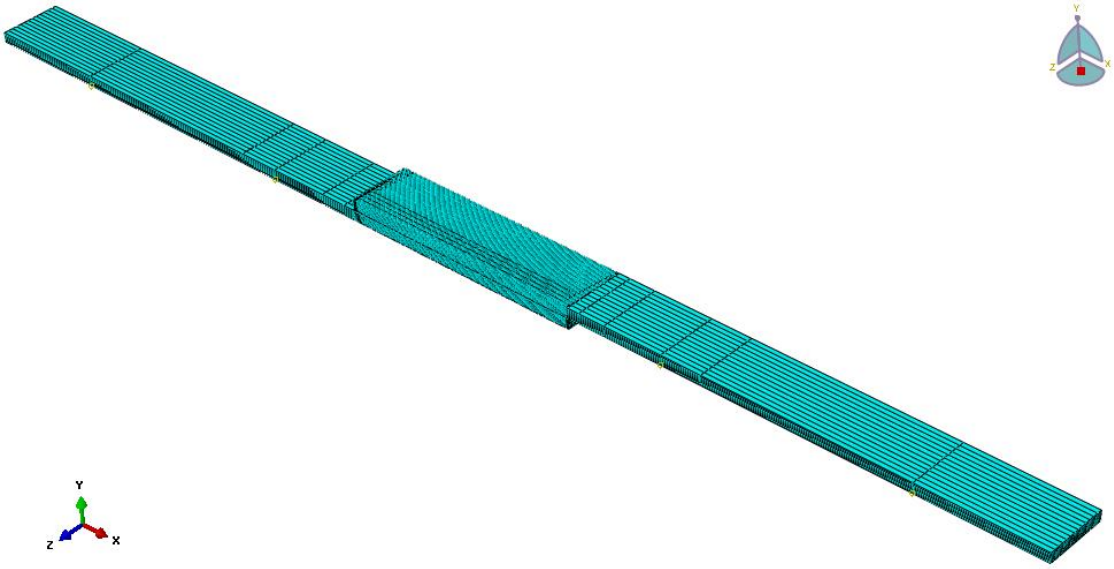

Figure 68- Total finite element mesh.

The final mesh was formed by a total of 105248 elements and 119406 nodes. The overlap area had 104000 elements and 119238 nodes.

5. Results

In this section the results obtained from the experimental tests and from the finite element analysis are presented. These results are compared and interpreted.

5.1 Experimental

The instrumented adhesive joints were submitted to loading cycles between 200 N and 5000 N. A load cell of 5 kN was used. Figure 69 shows an excerpt of a test realized.

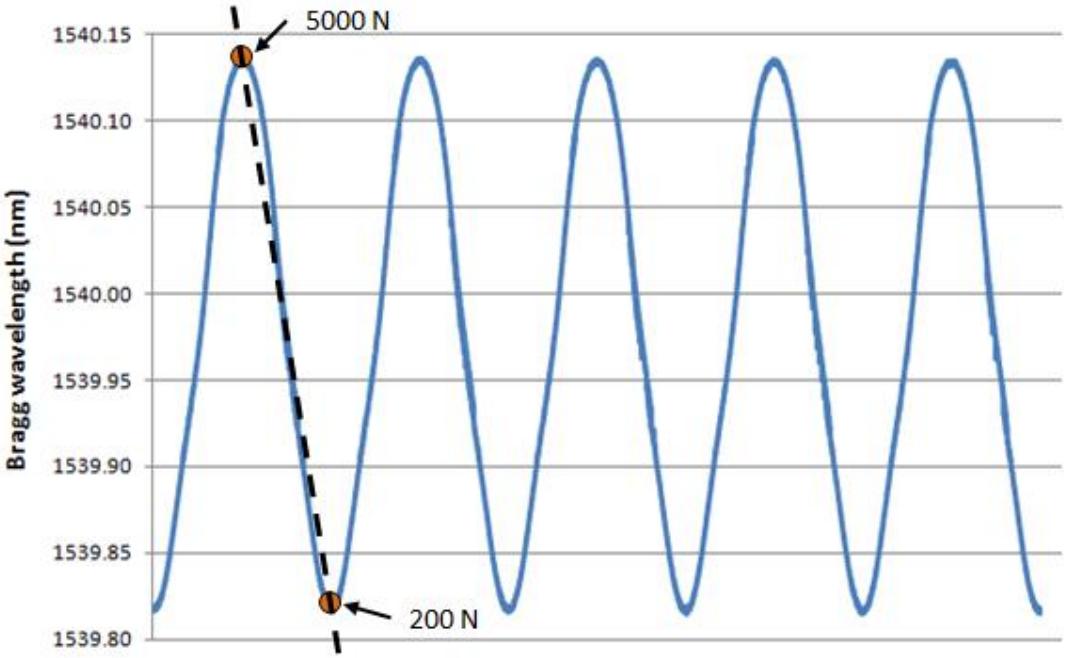

Figure 69- Excerpt of a test showing the variation of Bragg wavelength with time. Load values are superimposed.

As represented in Figure 69, the maximum value of the Bragg wavelength corresponds to the maximum applied load (5 kN) and, consequently to the maximum deformation experienced by the adhesive joint.

After determining the Bragg wavelength shift and, applying the calibration curve of the fiber Bragg sensor provided by Richter-Trummer et al. 2010, [28] the deformation is then obtained (Figure 70).

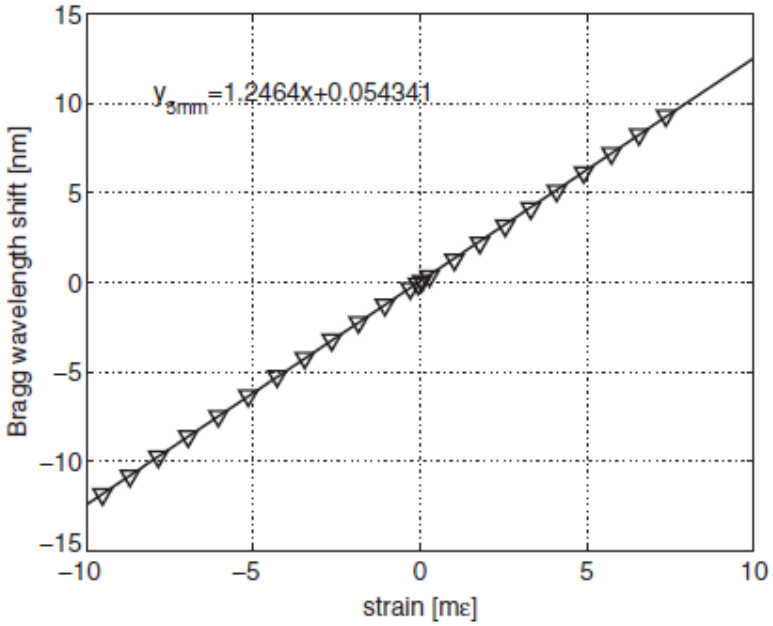

Figure 70- FBG sensor calibration curves for FBG 5 mm long gratings [28].

The calibration curve used is not the same presented in Figure 70. The curve shown has an additional correction value in the vertical axis, required by the measurement device used in those tests. For the experimental work in this thesis, there was no correction factor and the temperature was kept constant during the experimental tests.

There is an additional difference between the experimental procedure used to obtain the calibration curve shown in Figure 70 and the experimental work in this thesis. The curve was obtained for a sensor bonded with cyanoacrilate to the surface of an aluminum plate while in this thesis the sensor was embedded in the adhesive layer. This might account for some differences between the experimental and numerical data. However, a calibration technique that can be used as a reference for fibers inside the adhesive layer is not available. The use of calibration curves for surface bonded sensors is therefore a compromise to allow the calibration of sensors in the tested joints.

The calibration equation used is the following:

$$y_{5\,mm} = 1.2464x \qquad 5.1$$

where $y_{5\,mm}$ corresponds to the Bragg wavelength shift, in nm, and x is the deformation expressed in mε. The experimental results obtained are presented in Table 7. Only specimen 4

value corresponds to the measuring of a central sensor, all the others values correspond to sensors located on the extremities of the adhesive layer.

Table 7- Experimental axial strain results for tested specimens

	Axial Strain (mε)
Specimen 1	0.235
Specimen 2	0.276
Specimen 3	0.254
Specimen 4	0.189

The influence of the frequency of the loading cycles in the strain value read by the Bragg sensor was also tested. The same specimen with a single central sensor was submitted to loading cycles between 200N and 5000N and the frequency has taken the values 0.1 Hz, 1Hz and 10 Hz. Table 8 shows the results obtained.

Table 8- Axial deformation strains values for different frequency values.

Frequency (Hz)	Axial strain (mε)
0.1	0.159
1	0.189
10	0.151

The values presented in Table 8 do not show a clear connection between the load frequency and the values of axial strain read by the Bragg sensors.

After being submitted to loading cycles, the instrumented joints were tested up to failure at a crosshead rate of 1.5 mm/min.

Two joints were tested. One of the joints had a single sensor in the centre of the overlap area and the other joint had two, one in the centre of the overlap area and the other in the A position, as shown in Figure 71.

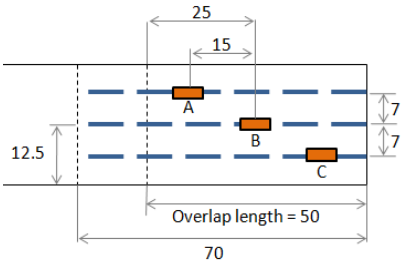

Figure 71- Sensors location.

The load-displacement curve from the tensile testing machine and the Bragg wavelength varying with time are represented in Figure 72 and Figure 73.

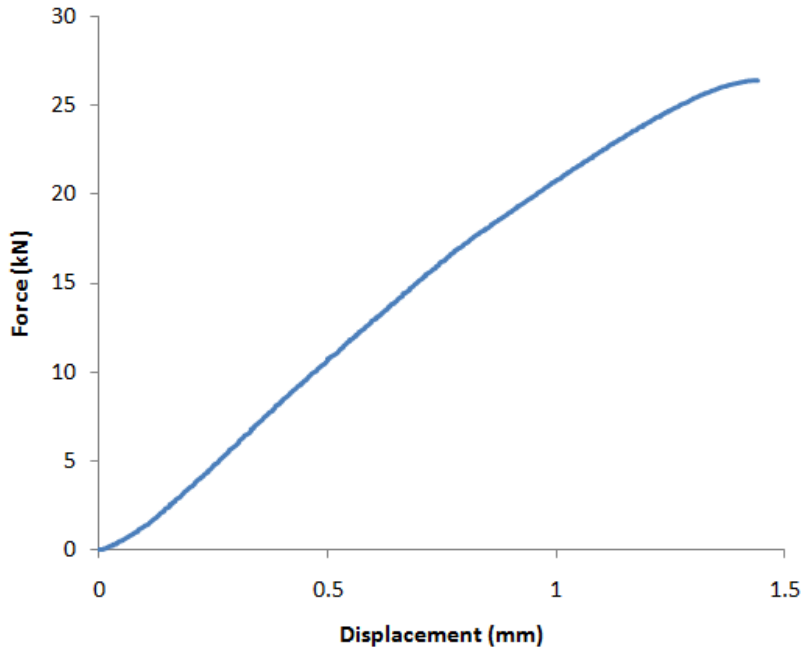

Figure 72- Load-displacement curve of an instrumented joint tested up to failure.

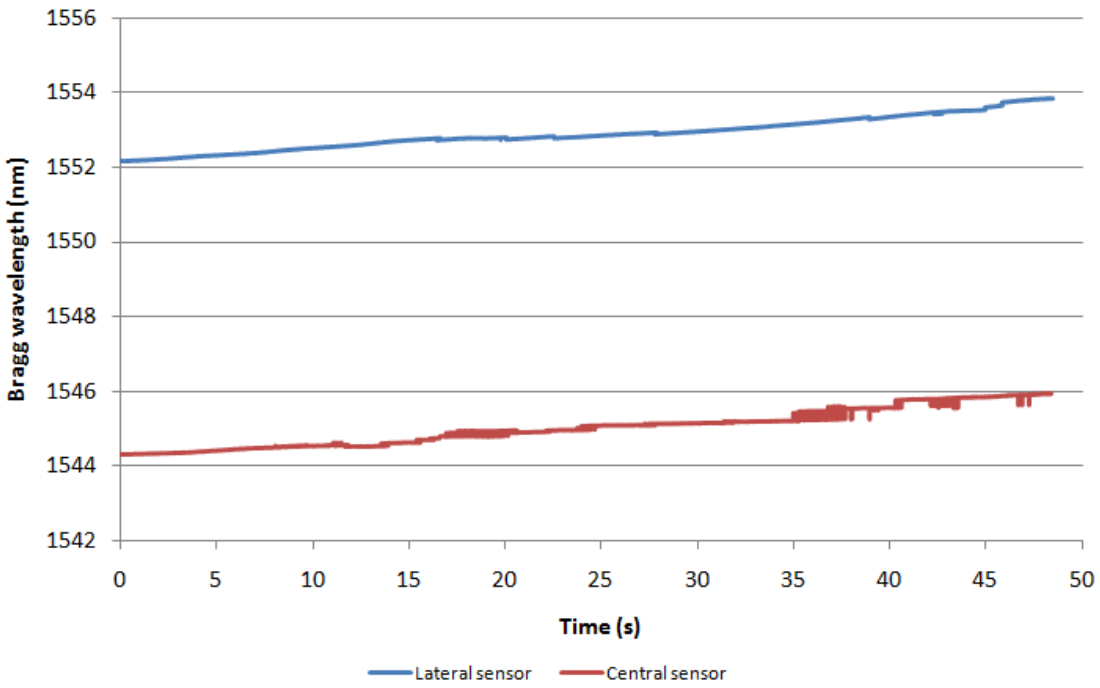

Figure 73- Bragg wavelength varying with time.

As expected, the strain values increase with time, as the applied loading rises. However the central sensor readings present some irregularities which can be related to the occurrence of sliding of the optical fiber inside the adhesive layer.

An accurate relationship between the loading applied by the test machine and the Bragg sensor signal could not be established as the two data sources (testing machine and BraggMETER) were not synchronized. Additionally, these results cannot also be directly compared in terms of displacement, as the displacement values given by testing machine are relative to the movement of the machine crosshead and not necessarily the displacement that is effectively applied to the specimen. To obtain an accurate picture of the relationship up to failure of the Bragg sensors and the loading/displacement of the adhesive joint it would be necessary to instrument the specimen with clip-on a strain gauge. This data would allow verifying the accuracy of the plastic finite element model up to the failure load. As a result, this work does not present results for the finite element analysis up to failure.

5.2 2D simulation results

Deformation values for the 2D simulation were not obtained by measuring the deformation of a single selected node but were instead the result of averaging the deformation values of a number of nodes located around an intended measurement point. This averaging is necessary due to the nature of Bragg sensors, which have a minimum measuring length of 5 mm.

This averaging process was done in two directions, vertically and horizontally for each measurement point. Nodes in the boundary of the adhesive layer were not considered for the vertical averaging as their deformation values are very dissimilar when compared to those located inside the adhesive layer. In the horizontal direction, the results obtained are an average between the deformation values determined for the nodes considered to be inside the length of a sensor (5 mm).

All axial strain values obtained with the finite element simulation model were taken at an applied load of 5 kN.

Table 9 shows the axial strain values obtained for the three points of interest, Figure 74.

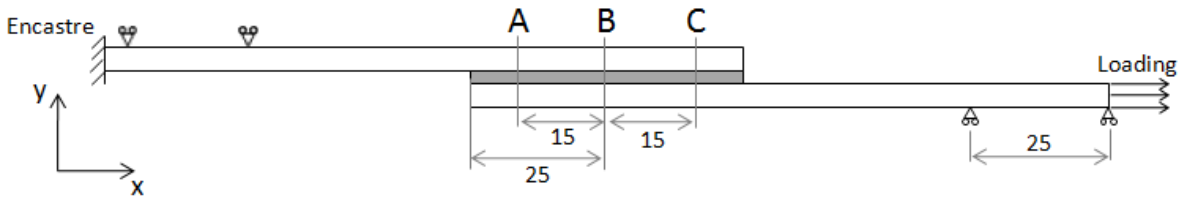

Figure 74- Sensors location in the longitudinal direction (not in scale, dimensions in mm).

Also these values were obtained by an applied load of 5 kN to a plastic finite element analysis and are expressed in mε.

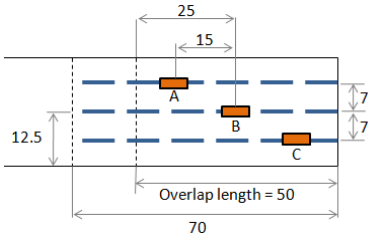

Table 9- 2D simulation values

Analyzed point	A	B	C
Axial strain (mε)	0.259	0.247	0.377

5.3 3D simulation results

As happened in the 2D simulation, the deformation values for the 3D simulation were not obtained by measuring the deformation of a single selected node but were instead the result of averaging the deformation values of a number of nodes located around an intended measurement point. The averaging process was exactly the same used in the 2D simulation and which was already described.

The axial strain values obtained with this 3D finite element simulation model were taken at an applied load of 5 kN. Table 10 shows the axial strain values obtained with a plastic finite element analysis for the three points of interest.

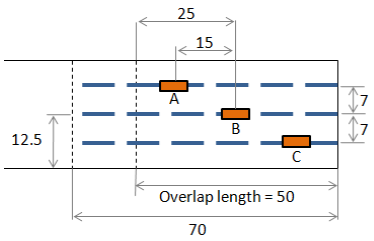

Table 10- 3D simulation values

Analyzed point	A	B	C
Axial strain (mε)	0.284	0.270	0.407

Figure 75 represents the axial strain distribution along the overlap length for an applied load of 5 kN. Two dimensional and three dimensional cases are represented. All values were obtained by a plastic finite element analysis and are expressed in mε.

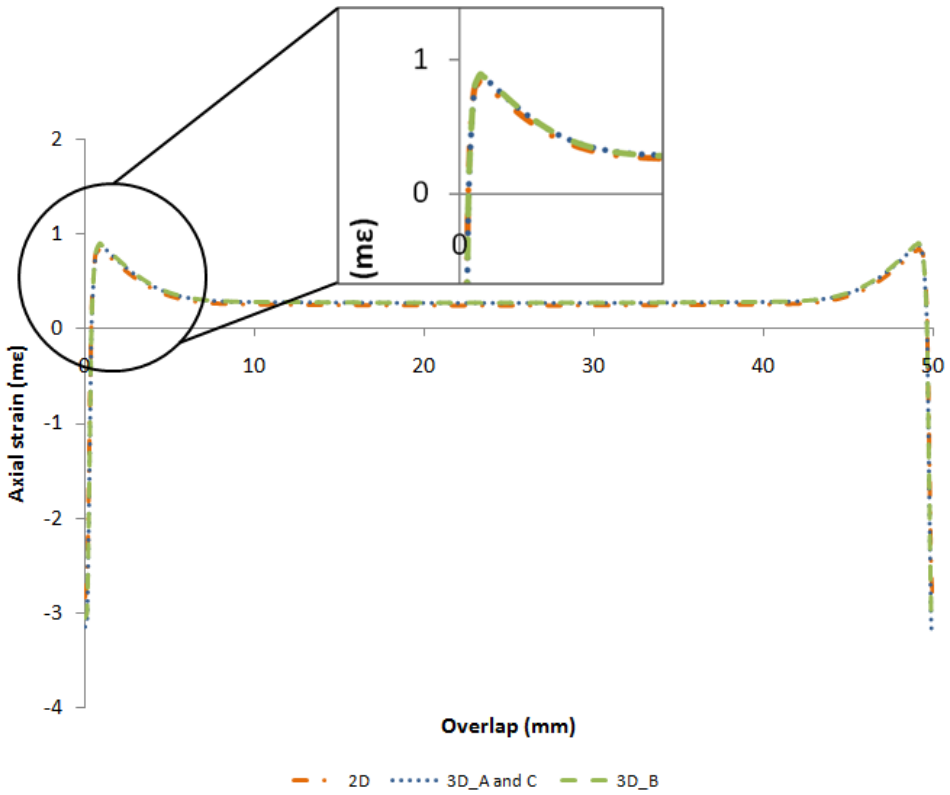

Figure 75- Axial strain distribution along the overlap length for 2D and 3D plastic analysis for an applied load of 5 kN.

The graph shows no significant difference between the strain distributions of the two finite element models that were studied.

5.4 Comparison between experimental and numerical results

Table 11 summarizes the experimental and the numerical values obtained during this work. The deviation percentages shown were calculated using the experimental strain values as reference.

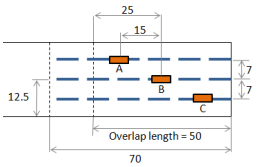

Table 11- Comparison between experimental and numerical strain values (values in mε).

Analyzed point	Experimental	2D plastic	2D difference (%)	3D plastic	3D difference (%)
A	0.235	0.259	10.2	0.284	20.9
B	0.189	0.247	30.6	0.270	42.9
C	0.254	0.377	48.4	0.407	60.2

According to Table 11, there is some discrepancy between some experimental and numerical results. Using the experimental strain values as reference, the finite element models return

strain values which can be up to 60% higher. The smallest difference is 10.2%, which is satisfactory, however most other measurement have a large difference. The two dimensional model proved to be slightly more accurate.

There are some possible reasons for these differences between experimental and numerical results. The first is the calibration procedure of the fiber. The calibration equation was obtained for a sensor bonded to an aluminium surface, which differs from the method used in this work. The other possibility is relative to an error in the mechanical properties introduced in the finite element model. The adhesive used is still being mechanically characterized and as such there are still some problems in obtaining reliable mechanical properties.

5.5 X-ray analysis

It is very important to have a non-destructive and easy technique that allows the inspection of the optical fiber alignment inside the adhesive layer. Initially, joints with steel substrates and with fibers embedded in the adhesive layer were submitted to x-ray analysis in order to observe the alignment of optical fibers inside the adhesive layer.

These initial tests did not provide useful results. The steel substrates were opaque to the x-rays and the images did not allow seeing anything inside the adhesive layer.

It was decided to produce a set of joints using substrates made of a CFRP. Being a material widely used in the aerospace industry, it is likely that Bragg sensors could be implemented in composite structures.

The CFRP joints were manufactured with the same geometry of the steel joints. The only difference was the substrate thickness which was 2.4 mm.

Figure 76 shows an X-ray of the overlap area of a CFRP specimen.

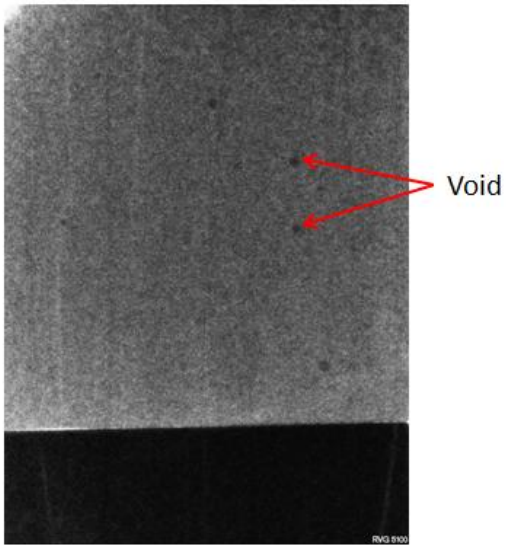

Figure 76- X-ray of the overlap area of a CFRP specimen.

As it can be observed, although the x-rays penetrate the substrates, fibers cannot be distinguished from the adhesive, as the fibers are transparent to the x-rays. The specimen was placed in a solution intended to increase the contrast of the objects but this liquid could not penetrate inside the adhesive layer and make the fibers visible. It is therefore concluded that this technique cannot be used to control the embedded fibers.

As shown in Figure 76, the X-ray is useful to assess the number of voids and defects on the adhesive layer. The joints produced were demonstrated to have a very small amount of defects, proving the effectiveness of the manufacturing method.

6. Conclusions

During the course of this work, a procedure for introducing optical fibers inside adhesive layers was successfully developed. It was found that it is extremely important to keep the fibers as straight as possible and a very simple fiber pre-tensioning mechanism was developed to that purpose. This method works satisfactorily with optical fibers. However, when the fibers are etched with Bragg sensors they become extremely fragile and frequently break during the joint manufacture process. Therefore, it is recommended to use fibers that have been recoated with a protective finish immediately after the Bragg sensor etching process. Alternatively, an auxiliary external mechanism can also be designed to keep the fibers tensioned and immobile during the whole bonding process. Due to time constraints this system could not be implemented in this work's procedures.

Additionally, the viscosity and the thermal contraction coefficient of the adhesive are two parameters which should also be considered. Due to the high fragility demonstrated by the silica fiber core, the adhesive selected should have a low thermal contraction coefficient, in order to avoid its breaking during the curing process.

The comparison between experimental and numerical results showed a relatively small discrepancy. As mentioned in the previous section of this work, the possible reasons for this difference might be related with the calibration procedure of the Bragg sensors as well as unreliable mechanical properties used in the finite element model. The results also did not demonstrate the existence of influence of loading rate in the strain values read by the sensor.

7. Future Work

- An alternative fiber tensioning mechanism should be introduced to specimen manufacturing procedure;
- The procedure should be tested with different adhesives and substrates with distinct mechanical properties;
- Obtain a new Bragg sensor calibration equation, more appropriate for the conditions where the fiber is installed in this work;
- Use a clip gauge extensometer during a test to failure, to allow comparison with the finite element models.
- Perform additional mechanical testing, varying and testing the influence of more parameters such as loading rate, temperature, fatigue cycling, etc.

8. References

1. **da Silva, L. F. M., de Magalhães, A. G. and de Moura, M. F. S. F.** *Juntas Adesivas Estruturais.* Porto : Publindústria, 2007.

2. **Jumbo, F., et al.** Experimental and numerical investigation of mechanical and thermal residual strains in adhesively bonded joints. *Strain.* 4, 2007, Vol. 43, pp. 88-104.

3. **Gomes, J. F. S.** *Mecânica dos sólidos e resistência dos materiais.* Porto : Edições INEGI, 2004.

4. **Fein, Howard.** Holographic Interferometry: Nondestructive tool. *The Industrial Physicist.* 1997.

5. **Vaz, M. and Gomes, J. F. S.** *Sebenta da disciplina Mecânica Experimental.*

6. *http://en.wikipedia.org/wiki/Neutron_diffraction.* [Online] [Accessed: April 5th 2011.]

7. **Frazão, O., et al.** *Sensores de Bragg em Fibra Óptica.*

8. **da Silva, L. F. M., et al.** Alternative methods to measure the adhesive shear displacement in the thick adherend shear test. *Journal of Adhesion Science and Technology.* 1, 2008, Vol. 22, pp. 15-29.

9. **Banea, M. D. and da Silva, L. F. M.** The effect of temperature on the mechanical properties of adhesives for the automotive industry. *Proc. IMechE Part L: J. Materials: Design and Applications.* 2, 2009, Vol. 224, pp. 51-62.

10. *http://pt.wikipedia.org/wiki/Fibra_%C3%B3ptica.* [Online] [Accessed: February 25th 2011.]

11. *www.knowledgerush.com.* [Online] [Accessed: March 6th 2011.]

12. *http://en.wikipedia.org/wiki/Total_internal_reflection.* [Online] [Accessed: Februay 25th 2011.]

13. *static.howstuffworks.com.* [Online] [Accessed: March 6th 2011.]

14. *http://www.unc.edu.* [Online] [Accessed: March 3rd 2011.]

15. *http://informatica.hsw.uol.com.br.* [Online] [Accessed: March 2nd 2011.]

16. **Maul, J. and kipp, T.** *Sensing of Surface Strain with Flexible Fiber Bragg Strain Gages.* Germany : HBM GmbH.

17. **Betz, D. C., et al.** Structural Monitoring Using Fiber-Optic Bragg Grating Sensors. *Structural Health Monitoring.* 2, 2003, Vol. 2, pp. 145-152.

18. **Ferreira, L. A., et al.** *Redes de Bragg em fibra óptica- Contribuições para o desenvolvimento de uma tecnologia revolucionária em monitorização estrutural.*

19. *http://www.fibersensing.com.* [Online] [Accessed: April 8th 2011.]

20. *http://zone.ni.com.* [Online] [Accessed: March 6th 2011.]

21. **Quintero, S. M. M.** *Aplicações de Sensores a Rede de Bragg em Fibras Ópticas na Medição de pH e Deformação de Filmes Finos de Alta Dureza.* Rio de Janeiro : Pontifícia Universidade Católica de Rio, 2006.

22. *http://t1.gstatic.com.* [Online] [Accessed: April 7th 2011.]

23. *http://www.crridom.gov.in.* [Online] [Accessed: April 7th 2011.]

24. **da Silva, L. F. M. and Lopes, M. J. C. Q.** Joint strength optimization by the mixed-adhesive technique. *International Journal of Adhesion & Adhesives.* 5, 2009, Vol. 29, pp. 509-514.

25. **Campilho, R. D. S. G., de Moura, M. F. S. F. and Domingues, J. J. M. S.** Stress and failure analyses of scarf repaired CFRP laminates using a cohesive damage model. *Journal of Adhesion Science and Technology.* 9, 2007, Vol. 21, pp. 855-870.

26. **Thorlabs.** *Guide to Connectorization and Polishing Optical Fibers.* 2007.

27. **Corp., Dassault Systemes Simulia.** *Abaqus Documentation Version 6.10-10.* 2010.

28. **Richter-Trummer, Valentin, et al.** Fibre Bragg grating sensors for monitoring the metal inert gas and friction stir welding processes. *Measurement science and technology.* 8, 2010, Vol. 21, pp. 1-8.